

Highlights

HydroGEM: A Self-Supervised Zero Shot Hybrid TCN-Transformer Foundation Model for Continental Scale Streamflow Quality Control

Ijaz Ul Haq, Byung Suk Lee, Julia N. Perdrial, David Baude

- Continental-scale foundation model trained on 3724 USGS sites with 6.03 million sequences
- Two-stage self-supervised pretraining with synthetic anomaly injection for detection
- Achieves $F1 = 0.792$ detection accuracy and 68.7% reconstruction-error reduction
- Zero-shot transfer to Canadian ECCC stations shows cross-national generalization
- Human-in-the-loop design for operational quality control workflows

HydroGEM: A Self-Supervised Zero Shot Hybrid TCN-Transformer Foundation Model for Continental Scale Streamflow Quality Control

Ijaz Ul Haq^{a,b,*}, Byung Suk Lee^a, Julia N. Perdrial^{c,b}, David Baude^b

^a*Department of Computer Science, University of Vermont, Burlington, VT, USA*

^b*Water Resources Institute, University of Vermont, Burlington, VT, USA*

^c*Department of Geography and Geosciences, University of Vermont, Burlington, VT, USA*

Abstract

Advances in sensor networks have enabled real-time, high-resolution stream discharge monitoring from in-situ gauges, yet persistent sensor malfunctions and data quality issues limit their utility. Manual quality control by expert hydrologists—while essential for maintaining data integrity—creates a bottleneck that delays scientific and operational use of these observations and cannot scale with networks generating millions of measurements annually. To address this gap, we introduce HydroGEM (Hydrological Generalizable Encoder for Monitoring), a foundation model for continental-scale streamflow quality control designed to support human expertise rather than replace it. HydroGEM uses a two-stage training approach: self-supervised pretraining on 6.03 million clean sequences from 3,724 USGS stations learns general hydrological representations, followed by fine-tuning with synthetic anomalies for detection and reconstruction. A hybrid Temporal Convolutional Network–Transformer architecture (14.2M parameters) captures both local temporal patterns and long-range dependencies, while hierarchical normalization handles learning across six orders of magnitude in discharge. On a held-out test set of 799 stations with 18 expert-validated anomaly types, HydroGEM achieves $F1 = 0.792$ for detection and 68.7% reconstruction-error reduction, outperforming the strongest baseline by 36.3%. Zero-shot transfer to 100

*Corresponding author

Email addresses: ihaq@uvm.edu (Ijaz Ul Haq), bslee@uvm.edu (Byung Suk Lee), jperdria@uvm.edu (Julia N. Perdrial), dbaude@uvm.edu (David Baude)

Environment and Climate Change Canada stations—unseen during training—yields $F1 = 0.586$, demonstrating cross-national generalization. The model maintains consistent detection across correction magnitudes (1–100%) and aligns with operational seasonal patterns, with peak flagging rates during winter ice-affected periods matching hydrologists’ correction behavior. Architectural separation between simplified training anomalies and complex physical-space test anomalies confirms that performance reflects learned hydrometric principles rather than pattern memorization.

Keywords: Streamflow Quality Control, Foundation Model, Anomaly Detection, Self-Supervised Learning, Hydrological Monitoring, Deep Learning, Zero-Shot Transfer

1. Introduction

Real-time hydrological monitoring networks provide essential observations for water resources management, flood forecasting, ecosystem protection, and climate change adaptation [1, 2, 3]. The United States Geological Survey operates more than 10,000 stream gauging stations that collectively produce millions of paired discharge and stage measurements each month, forming the backbone of decision-making across federal, state, and local agencies [4, 3]. High-frequency sensor data are only as useful as their quality, and without timely, accurate quality control, the growing volume of observations becomes a bottleneck rather than a resource [5].

Advances in sensor technology, telemetry, and network infrastructure have dramatically expanded the spatial and temporal density of hydrological monitoring. Modern gauging stations transmit stage and discharge at sub-hourly intervals, enabling near-real-time flood warnings, reservoir operations, and ecological flow management. Yet despite these technological improvements, raw sensor data remain inherently imperfect. Even in well-maintained monitoring networks, physical sensors inevitably experience drift, fouling, ice effects, rating-curve shifts, clock errors, and transmission failures, producing intermittent gaps or anomalies in the data [6, 7]. These issues are an inherent part of real-world sensing, where the central challenge is ensuring fast, reliable quality control of the data they generate.

Traditional quality control in hydrological monitoring combines manual expert review with rule-based automated checks [8, 9, 10]. Commercial systems such as AQUARIUS implement configurable range checks, rate-of-

change thresholds, and statistical comparison filters, providing standardized workflows and audit trails [8]. Open-source frameworks like SaQC advance reproducibility through sequential test configurations and traceable quality flags [9]. However, rule-based approaches face fundamental limitations: fixed thresholds require site-specific calibration and capture only obvious outliers. Context-dependent anomalies—such as ice effects that preserve plausible values but bias discharge [11], gradual sensor drift within historical ranges [12], or rating curve shifts after channel-altering floods [13]—often evade detection. Multivariate relationships between discharge and stage, critical for identifying coupled sensor failures or unit conversion errors, are difficult to encode in rule-based systems. As monitoring networks expand and temporal resolution increases, manual calibration becomes prohibitively expensive.

Current operational practice therefore relies heavily on domain experts who visually inspect time series, interpret stage–discharge relationships, and apply site-specific judgment [5, 14]. While this expert-driven workflow produces high-quality records, its manual nature cannot keep pace with expanding monitoring networks and rising data frequency. The resulting bottleneck stems not from insufficient expertise but from the growing mismatch between data volumes and the capacity for timely human review.

Recent advances in machine learning offer a promising path toward more efficient and scalable hydrologic data quality control. Modern models can process continuous data streams, capture subtle temporal dependencies, and operate consistently across large station networks—capabilities well aligned with the needs of contemporary monitoring systems. In principle, such methods could provide rapid, reliable quality screening across thousands of sites.

Classical anomaly detection methods have been applied to environmental monitoring with mixed success. Statistical approaches (z-score tests, ARIMA residuals), distance-based methods (k-nearest neighbors, isolation forests), and one-class classifiers (one-class SVM, autoencoders) provide baseline capabilities [15, 16]. Recent applications include wavelet-based multi-resolution analysis for river stage [17] and comparative evaluations of isolation forests versus one-class SVM for groundwater monitoring, where OCSVM achieved 88% precision on synthetic data [16].

Deep learning approaches show stronger performance by capturing complex temporal dependencies. LSTM networks and Transformer attention mechanisms excel at modeling long-range patterns in time series [18, 19]. Temporal Convolutional Networks enable efficient parallel processing with exponentially large receptive fields [20]. Autoencoders—including variational

and LSTM-augmented variants—detect anomalies via reconstruction errors [21, 22]. Generative Adversarial Networks improve robustness through learned representations of normal data distributions [23]. Synthetic anomaly generation has emerged as a key technique for training when domain-specific labeled data are unavailable [24].

Translating this potential into practice, however, is challenging because continental-scale deployment faces two fundamental obstacles. First, hydrological systems are extremely heterogeneous: discharge spans six orders of magnitude across sites, and flow generation mechanisms vary with climate, physiography, and human modification [4, 2, 25]. Models typically train and evaluate on individual sites or small regional datasets (often fewer than 50 sites), failing to capture the extreme heterogeneity spanning snowmelt-dominated montane systems to ephemeral desert washes to regulated lowland rivers. Transfer learning across such diverse regimes remains largely unexplored in hydrological anomaly detection. Second, labeled anomaly datasets are scarce. Agency quality flags are not designed as ground truth labels that cleanly separate sensor faults from physical phenomena, and comprehensive labeled datasets across thousands of sites do not exist [7, 15].

Foundation models—large networks pretrained on massive datasets with self-supervised objectives, then transferred to diverse downstream tasks—provide a path forward [26, 27]. In weather and climate science, ClimaX demonstrated that transformers pretrained on heterogeneous climate reanalysis data with masked token prediction effectively transfer to forecasting, downscaling, and multi-variable prediction across spatiotemporal scales [28]. Weather foundation models including FourCastNet [29], GraphCast [30], and Pangu-Weather [31] now achieve medium-range forecast skill competitive with operational numerical weather prediction at orders of magnitude lower computational cost. Industrial-scale efforts such as IBM/NASA’s Prithvi WxC (2.3B parameters) [32] and Oak Ridge’s ORBIT (>100B parameters) [33] are extending this paradigm to multi-variable Earth system prediction.

In hydrology, Kratzert and colleagues pioneered multi-basin learning by training LSTM networks across hundreds of catchments using the CAMELS dataset [4], demonstrating that models learn generalizable runoff generation processes that transfer to ungauged basins. Subsequent work confirmed that diverse training across basins improves predictions despite regional hydrological variation [34]. Remote sensing foundation models pretrained on satellite imagery have shown strong transfer to environmental monitoring tasks [35]. Recent perspectives advocate for foundation models as assistive tools in hy-

drometeorology when developed with appropriate domain constraints [35].

Yet foundation model principles have not been systematically applied to quality control for *in situ* sensor networks. This gap reflects unique challenges: extreme scale heterogeneity (six orders of magnitude in discharge within a single dataset, requiring specialized normalization); irregular multi-site time series (non-gridded data with site-specific rating curves, instrument types, and operational protocols); real-time deployment constraints (inference must operate without access to ground truth); deploy-safe requirements (the model must not corrupt valid data—a failure mode unacceptable in operational settings); and human oversight mandates (agencies require interpretable outputs, uncertainty quantification, and audit trails for regulatory compliance).

Our approach addresses these limitations by integrating advances from multiple domains. From foundation models [28, 29], we adopt self-supervised pretraining on massive unlabeled datasets. From large-sample hydrology [4, 34], we use multi-site learning for cross-basin transfer. From recent deep learning work [27, 24], we use synthetic anomaly injection for task-specific fine-tuning. From operational QC systems [8, 9], we incorporate human-in-the-loop workflows and audit requirements. The result is a system that learns multivariate patterns from continental-scale data, enabling context-aware detection without manual threshold tuning while preserving the human-in-the-loop workflows that agencies require.

To address these challenges, we introduce **HydroGEM** (Hydrological Generalizable Encoder for Monitoring), a self-supervised foundation model for continental-scale streamflow quality control. HydroGEM qualifies as a foundation model because it: (1) trains on massive diverse data (3,724 sites spanning six orders of magnitude in discharge), (2) uses self-supervised pretraining to learn general hydrological representations, (3) shows zero-shot transfer to unseen sites and countries, and (4) uses a modular architecture that allows task-specific adaptation.

HydroGEM uses a two-stage training approach. **Stage 1** pretrains a hybrid TCN-Transformer backbone on 6.03 million clean sequences from 3,724 USGS sites using masked reconstruction. A hierarchical normalization scheme—combining log transforms, site-specific standardization, and explicit scale embeddings—allows learning across extreme magnitude ranges while preserving physically meaningful scale structure [36]. **Stage 2** fine-tunes the pretrained backbone with a detection head using on-the-fly synthetic anomaly injection rather than curated labels [27, 24]. The training injector

applies simplified corruptions (drift, spikes, flatlines, dropouts, clock shifts) in normalized space to encourage learning of fundamental hydrometric consistency principles rather than memorization of specific anomaly signatures. Clean data preservation exceeds 97%, ensuring the model does not corrupt valid observations.

Evaluation emphasizes generalization across three dimensions. We construct a synthetic test set of 799 USGS sites (completely unseen during training) with expert-validated anomalies that are deliberately more complex than training corruptions, creating a four-axis separation (geographic, mathematical, temporal, parameter) that prevents pattern memorization. On this held-out set, HydroGEM achieves 0.70 F1 for anomaly detection and reduces reconstruction error by 70% relative to injected corruptions—though suggested corrections require expert review [10] before operational use. For real-world validation, we evaluate zero-shot transfer to 100 Environment and Climate Change Canada (ECCC) sites using weak labels derived from operational corrections. Reconstructions show promising alignment with agency corrections in several cases, though direct comparison is limited by differences in correction methodology between USGS and ECCC workflows. This cross-national evaluation tests whether the learned representations transfer beyond the training data source [4, 37].

HydroGEM is designed for human-in-the-loop workflows: a three-tier flagging system passes high-confidence clean data with minimal review, prioritizes uncertain observations for expert inspection, and provides suggested reconstructions with uncertainty estimates. All outputs include provenance information suitable for audit and feedback, supporting hydrologist expertise [10, 5, 14].

In summary, this work advances hydrological quality control through five contributions:

1. A continental-scale foundation model trained on 3,724 USGS sites with 6.03 million sequences—an order of magnitude larger than prior multi-site hydrological studies.
2. A two-stage training approach combining self-supervised pretraining on clean data with synthetic anomaly injection for detection and reconstruction, reducing dependence on labeled anomalies.
3. Hierarchical normalization enabling learning across six orders of magnitude while preserving scale-dependent physical behavior.

4. Expert-validated evaluation with 18 anomaly types and rigorous site-level partitioning ensuring zero-shot generalization assessment, achieving 0.70 F1 detection and 70% error reduction in suggested reconstructions.
5. Demonstrated cross-national transfer from USGS (USA) to ECCC (Canada) data, validating learned representations beyond training distribution.

Table 1 contrasts HydroGEM with related approaches across key dimensions.

Table 1: Positioning HydroGEM relative to related approaches

Approach	Sites	Self-sup.	Zero-shot	Synthetic	Recon.	Deploy-safe
Rule-based QC [8, 9]	Any	N/A	N/A	No	Manual	Yes
Single-site ML [19, 22]	1–10	Varies	No	Sometimes	Varies	No
Multi-basin hydro [4]	100–500	No	Yes	No	No	N/A
Weather FM [28, 29]	Gridded	Yes	Yes	No	No	N/A
HydroGEM	3,724	Yes	Yes	Yes	Suggested	Yes

Table ?? summarizes key technical terms used in this paper.*** **Ijaz,**
can we refer to the terminology table as a LaTeX table here?

Terminology

- **Clean data:** USGS approved records with quality code ‘A’ (verified and approved by USGS hydrologists as accurate representations of observed conditions; used for Stage 1 training)
- **Masked data:** Clean data with random timesteps hidden for self-supervised reconstruction (Stage 1)
- **Corrupted data:** Clean data with synthetic anomalies injected (Stage 2 fine-tuning)
- **Anomalous data:** Real operational data requiring correction (deployment target)
- **Suggested reconstruction:** Model-proposed correction requiring hydrologist approval
- **Stage/Gage height:** Water surface elevation measured at the gauging station, typically in feet
- **Discharge:** Volume of water flowing past a point per unit time, typically in cubic feet per second (ft^3/s)
- **Rating curve:** Empirical relationship between stage and discharge at a specific site

2. Data and Evaluation Framework

Our evaluation strategy combines three data sources (Figure 1): (1) a continental-scale USGS corpus for foundation model pretraining, (2) synthetic test sets with expert-validated anomalies for controlled generalization assessment, and (3) real-world Canadian stations for zero-shot cross-national transfer validation. This multi-tiered design allows rigorous evaluation under both controlled conditions with known ground truth and operational settings with genuine quality control challenges.

2.1. Foundation Training Corpus

2.1.1. USGS Streamflow Archive

We assembled a continental-scale dataset from 5,321 USGS streamgaging stations via the National Water Information System (NWIS) [38], covering January 2000 through December 2024. For each station, we selected the best 10-year continuous period with high-quality paired discharge (Q) and stage

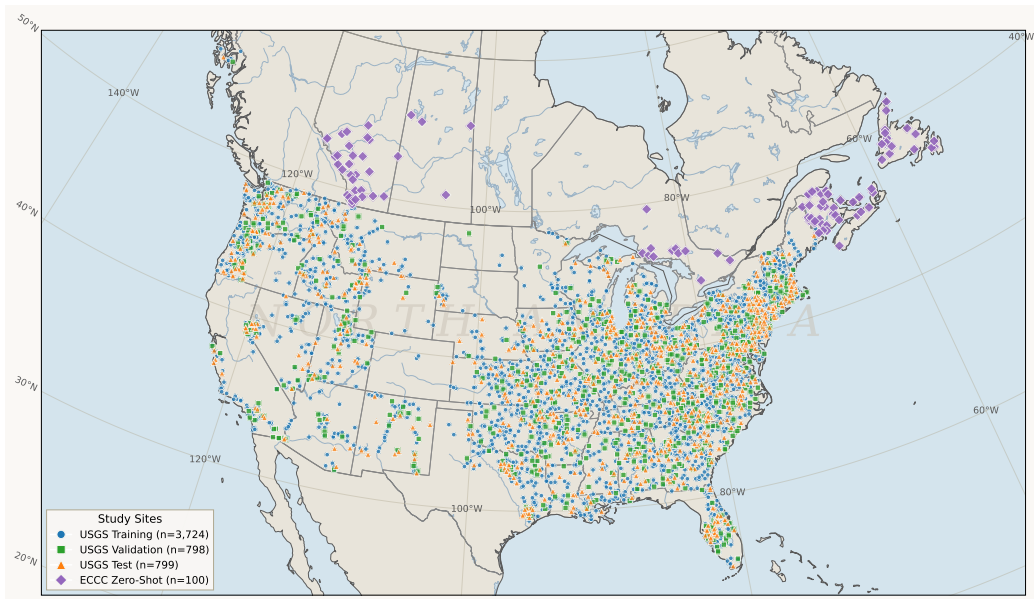


Figure 1: Geographic distribution of study sites. USGS stations are split into training ($n=3,724$), validation ($n=798$), and test ($n=799$) sets with no geographic overlap. Canadian ECCC stations ($n=100$) were selected based on data completeness and quality criteria described in Section 2.4.2.

(*H*) observations. All records carry USGS qualification code ‘A’ (approved), distinguishing them from provisional data subject to revision. Instantaneous readings (typically 15-minute intervals) were aggregated to hourly resolution via arithmetic means for consistent temporal scale.

The 10-year site-specific selection strategy balances data quality, temporal depth, and infrastructure consistency. Post-2000 focus ensures modern instrumentation across the network, while 10-year spans capture multiple seasonal cycles and extreme hydroclimatic events (droughts, floods) essential for robust anomaly detection. This period also corresponds to relatively standardized USGS quality control protocols, reducing confounding institutional factors.

2.1.2. Spatial and Hydrologic Coverage

The network spans the conterminous United States, Alaska, and Hawaii (162.69°W to 67.32°W, 19.71°N to 61.71°N), providing true continental-scale geographic diversity. Drainage areas range from 0.03 to 932,800 km² (median 196 km²), consistent with scale-invariant river network organization. Gauge elevations span –69 m to 2,747 m (mean 467 m), capturing coastal, lowland, montane, and alpine monitoring sites.

This spatial coverage ensures exposure to principal North American flow generation mechanisms: snowmelt-dominated montane regimes, rainfall-dominated humid systems, mixed snow-rain transitional climates, ephemeral arid flows, and regulated downstream conditions [39]. Such hydrologic diversity is critical for developing transferable representations that generalize beyond specific flow regimes.

2.1.3. Quality Control and Preprocessing

We apply a multi-tier quality control protocol (detailed in Appendix Appendix D) ensuring training data integrity while preserving temporal coverage. Sites with < 90% completeness are excluded (removing 679 out of 6000 total). Retained sites undergo outlier detection (4σ threshold from monthly means), physical plausibility checks against rating curves [40], and temporal consistency validation.

Gap filling uses hierarchical strategies: linear interpolation for gaps ≤ 6 hours, exponential recession models [41, 42] for 6-24 hour gaps, and exclusion for gaps > 24 hours. This protocol retains 94.7% of potential sequences, with 89.3% containing no interpolation. Windows intersecting flagged spans are dropped, eliminating information leakage.

2.1.4. Dataset Partitioning

To assess generalization, we assign entire sites to a single partition, avoiding leakage of site-specific signatures [4]. The split allocates 70% training (3724 sites), 15% validation (798 sites), and 15% test (799 sites), preserving geographic coverage and proportional hydrologic region representation.

Continuous hourly series are segmented into 576-hour windows (24 days), capturing storm hydrographs, weekly patterns, and diurnal fluctuations while remaining tractable for transformers [43]. Asymmetric stride—48 hours for training (dense overlap maximizing data utilization), 192 hours for validation/test (reducing autocorrelation)—produces 6.03M training sequences, 0.32M validation, and 0.33M test sequences (Table 2).

Table 2: Foundation corpus statistics

Partition	Sites	Windows (M)	Length (h)	Stride (h)	Timesteps (M)
Training	3,724	6.03	576	48	3,470.59
Validation	798	0.32	576	192	185.98
Test	799	0.33	576	192	187.35
Total	5,321	6.67	576	—	3,843.92

2.2. Preprocessing Pipeline

2.2.1. Feature Engineering

At each timestep t for site s , the model observes $\mathbf{x}_t \in \mathbb{R}^{12}$ combining static descriptors, dynamic hydrology, and derived temporal context (Table 3). This compact design balances information richness, computational tractability, and operational constraints—specifically, we exclude meteorological forcings (precipitation, temperature) to maximize applicability to gauge-only deployment scenarios.

Static descriptors $\{\phi, \lambda, A_d, z_g\}$ provide coarse hydrograph controls through latitude (e.g., climatic gradients), longitude (e.g., continental position), drainage area (e.g., flashiness), and elevation (e.g., temperature lapse rates). **Dynamic variables** $\{Q, H\}$ constitute the core physical state, with stage encoding local geometry and backwater effects [44] invisible in discharge alone. **Derived features** include scale embeddings returning absolute variability information lost during standardization, cross-site ranks stabilizing learning across magnitude orders, and monthly anomalies expressing seasonal departures.

Table 3: 12-dimensional feature set composition

Category	Features	Dimension
Static basin	Latitude, longitude, drainage area, elevation	4
Dynamic hydrology	Discharge (Q), stage (H)	2
Scale embeddings	$\sigma_{\ln Q}$, $\sigma_{\ln H}$ (training std. dev. of log-transformed series)	2
Cross-site ranks	Ordinal position: $\text{rank}(A_d)/N$, $\text{rank}(z_g)/N$	2
Seasonal context	Monthly anomalies: $(Q - \mu_{Q,m})/\sigma_{Q,m}$, $(H - \mu_{H,m})/\sigma_{H,m}$	2
Total		12

2.2.2. Hierarchical Normalization

Hydrological magnitudes vary by six orders across sites (0.1 to 100,000 ft³/s), creating severe optimization challenges. Standard approaches fail: global standardization yields large-river dominance; site-specific alone loses cross-site comparability; min-max scaling suffers outlier sensitivity; raw units prevent convergence.

We introduce a three-tier hierarchical normalization (full mathematics in Appendix Appendix A) simultaneously achieving: (1) stable gradients across extreme heterogeneity, (2) zero train-test leakage, (3) exact physical unit recovery, and (4) scale-dependent information preservation.

Tier 1 - Logarithmic stabilization: Apply $Q^{(1)} = \ln(Q + \epsilon)$, $H^{(1)} = \ln(H + \epsilon)$ for approximately log-normal variables [45], linearizing rating curves and stabilizing variance.

Tier 2 - Site-specific standardization: Compute μ_s , σ_s exclusively from each site’s training data, then transform $\mathbf{x}^{(2)} = (\mathbf{x}^{(1)} - \mu_s)/(\sigma_s + \epsilon)$. For validation/test sites, substitute global training statistics, maintaining strict partition separation.

Tier 3 - Global clipping: Apply $\mathbf{x}^{\text{norm}} = \text{clip}(\mathbf{x}^{(2)}, -3, +3)$ to inputs only, retaining 99.7% of normal variation while preventing gradient explosion. Outputs denormalize without clipping.

Exact inverse: $\hat{y} = \exp[\hat{y}^{\text{norm}} \cdot (\sigma_s + \epsilon) + \mu_s] - \epsilon$ recovers physical units. Scale embeddings ($\sigma_{\ln Q}$, $\sigma_{\ln H}$) return absolute variability information enabling scale-dependent behavior (e.g., flashiness in small basins).

Rationale: The logarithm converts multiplicative noise to additive; site-specific standardization enables weight sharing without large-river dominance; clipping provides numerical stability; embeddings distinguish 10 ft³/s (small creek) from 10,000 ft³/s (large river) despite identical post-normalization

values. No single-tier normalization achieves all requirements for continental-scale learning.

2.3. Training-Time Anomaly Injection

Anomaly detection requires labeled corruption patterns, but manual annotation of 6M sequences is prohibitively expensive. We implement on-the-fly synthetic injection generating diverse patterns during stage 2 fine tuning for anomaly detection which is also a part of our training process.

Deliberate simplification philosophy: The training injector implements ~ 11 simplified patterns (spikes, drift, flatlines, dropouts, saturation, clock shifts, quantization, unit jumps, warping, splicing) applied in normalized log-space, deliberately less sophisticated than test anomalies. This design forces learning of fundamental hydrometric consistency principles (discharge-stage coupling, temporal smoothness, physical plausibility) rather than memorizing specific signatures. If training and test used identical patterns, strong performance could arise from pattern matching rather than genuine understanding. The training-test complexity gap creates a defensible generalization test.

Controlled coverage: Two-tier system assigns light corruption (60% probability, 5-15% coverage) or moderate (40% probability, 15-30% coverage) with iterative refinement ($\pm 3\%$ tolerance for light, $\pm 5\%$ for moderate), maintaining mean $15.2\% \pm 3.1\%$ across batches. Mixing: single-type (60%) teaches type-specific patterns; double-type (40%) teaches discrimination. Segments: $n \in [2, 4]$ with lengths $L \in [T/100, T/4]$ randomly positioned. Curriculum scheduling ramps injection probability from 0.2 (epochs 1-2) to 0.4 (thereafter). Complete implementation details in Appendix Appendix E.

2.4. Evaluation Datasets

2.4.1. Synthetic Test Set Design

Rigorous generalization assessment requires test data preventing memorization while probing genuine abstraction. We construct a synthetic test set from 799 held-out USGS sites with expert-validated anomalies spanning 18 consolidated types (Table 5). Four orthogonal separation axes between training and test distributions ensure strong performance requires learning fundamental hydrometric principles rather than pattern matching.

Geographic separation: Zero site overlap eliminates memorization of station-specific patterns. **Mathematical separation:** Each test anomaly

Table 4: Four-axis training-test separation strategy

Axis	Training	Test	Purpose
Geographic	3,724 sites	799 non-overlapping sites	Eliminate site memorization
Mathematical	Linear drift, basic off-sets	Exponential/sigmoid/polynomial; 3-4 variants per type	Require functional abstraction
Temporal	8-96 hour segments	Micro (3-58h), Meso (7-192h), Macro (72-520h)	Probe scale-invariant detection
Parameter	Coverage 10-32%, nominal strength	Coverage trimodal: 3-9% / 32-44% / 44-60%; Severity bimodal	Test distribution boundaries

type implements 3-4 equation variants (e.g., drift: linear, exponential, sigmoid, polynomial) producing similar visual patterns through different mechanisms. **Temporal separation:** Structured duration regimes (micro/meso/macro) spanning 3-520 hours, with macro extended to 520h based on expert feedback regarding ice persistence [46]. **Parameter separation:** Coverage and severity anti-overlap the training sweet spot, testing distribution boundaries.

Expert validation and taxonomy consolidation.. We assembled an HTML validation gallery with 8+ representative sequences per anomaly type, reviewed by domain experts using structured protocols (realism scoring, temporal validation, confound detection). Reviewers included a geoscience faculty member with extensive experience in water resources research and a research assistant from the Water Resources Institute at the University of Vermont with operational USGS internship experience examining real-world data quality issues. Based on systematic feedback, we consolidated to 18 types with field-relevance agreement (Table 5), categorized by confidence: high (9 types: dropout, flatline, spike, backwater, ice_backwater, drift, rating_drift, debris_effect, sedimentation), medium (4 types), low (4 types), and debated (retained with caveat). Complete consolidation mapping and expert feedback integration details appear in Appendix Appendix G.

Table 5: Consolidated anomaly taxonomy (18 types)

Category	Types	Confidence	Variants
Sensor failures	Dropout, flatline, spike	High	3-4 each
Hydraulic phenomena	Backwater, ice_backwater, debris_effect, sedimentation	High	3-4 each
Gradual degradation	Drift, rating_drift, sensor_fouling	High/Medium	3-4 each
Processing errors	Bias_step, time_misalignment, quantization	Medium/Low	3-4 each
Complex artifacts	Splice, warp, noise_burst, gate_operation	Low/Debated	3-4 each

Physical-space injection.. All test anomalies inject in denormalized physical space to respect actual discharge-stage coupling. The three-step process: (1) denormalize to physical units, (2) apply parametric transformations with hydraulic constraints (e.g., ice: $H' = H(1 + \alpha_{\text{ice}})$, $Q' = Q(1 - \beta_{\text{ice}})$ with $\alpha \sim U(0.15, 0.55)$, $\beta \sim U(0, 0.10)$), (3) renormalize with clipping. Single-type isolation (30% of sequences) enables per-type diagnostics; compound anomalies (70%, with 40% overlap probability) test discrimination. Complete injection implementation details, equation variants, and reproducibility protocols appear in Appendix Appendix F.

Rationale for synthetic evaluation.. Synthetic data provides defensible evaluation: deliberate separation prevents memorization; physical grounding ensures realism; multi-axis design probes distinct generalization modes; expert validation provides external validity; controlled conditions enable fine-grained diagnostics. Complementarity with operational validation (Section 2.4.2) provides stronger evidence than either alone—synthetic proves learned concepts, operational proves practical transfer.

2.4.2. Canadian Zero-Shot Transfer Evaluation

The USGS archive provides quality-controlled products but lacks systematic raw-vs-corrected record pairs exposing operational correction workflows. To test real-world transfer, we evaluate HydroGEM on Environment and Climate Change Canada (ECCC) stations distributing hourly raw and corrected unit values for both discharge and stage.

Zero-shot protocol: HydroGEM was trained exclusively on USGS sites and never fine-tuned on Canadian data. All experiments are strictly zero-shot, testing whether learned representations generalize across political boundaries, agencies, instrumentation protocols, and rating curve derivation methods.

Data preprocessing: We obtained ECCC unit value archives, aggregated to hourly resolution, and converted to imperial units (stage: m→ft via 3.28084; discharge: $\text{m}^3/\text{s} \rightarrow \text{ft}^3/\text{s}$ via 35.3147) matching USGS conventions. Temporal alignment ensured all four series (stage raw/corrected, discharge raw/corrected) available at each hourly timestep.

Quality filtering: To ensure meaningful evaluation, we applied hydrologically-motivated checks to corrected records: sufficient variability ($\text{CV} > 0.10$), monotonic rating ($\rho > 0.5$), reasonable exponent ($b \in [0.5, 10]$), moderate fit ($R^2 \geq 0.3$), valid data fraction ($\geq 70\%$), limited flatlines ($< 30\%$ differences

< 0.001 ft). Station-level filtering excluded sites losing > 5% timesteps. Detailed filtering protocols appear in Appendix Appendix H.

Weak label construction: We compute relative changes induced by operational correction: $\Delta Q_{\text{rel}} = |Q_{\text{corr}} - Q_{\text{raw}}|/(|Q_{\text{raw}}| + \epsilon)$, similarly for H . Timesteps with $\Delta Q_{\text{rel}} > 0.01$ or $\Delta H_{\text{rel}} > 0.01$ are marked anomalous ($y_{\text{corr}} = 1$), providing weak labels encoding where human expertise deemed raw data untrustworthy. The 1% threshold is intentionally conservative, capturing meaningful hydrograph adjustments.

These labels are “weak” because human editors may miss subtle anomalies or correct for operational reasons orthogonal to data quality (e.g., re-rating after channel changes). Nevertheless, they provide externally-validated ground truth unavailable in synthetic datasets. Pattern-based labels (local correlation deviations) complement correction-based labels, emphasizing multi-point segments where corrected hydrograph shape deviates from raw.

Site sampling: From all stations satisfying quality criteria, we randomly sampled 100 distinct stations for evaluation, ensuring representative out-of-sample behavior without cherry-picking. Window filtering required 10-40% correction fraction, identifying substantial but not overwhelming editing effort. For each site, we evaluate HydroGEM in pure zero-shot configuration, comparing binary anomaly masks against correction-based and pattern-based labels.

2.5. Summary

Our data preparation pipeline yields:

- **Foundation corpus:** 6.67M sequences (3.84B hourly timesteps) from 5,008 USGS stations (70/15/15 train/val/test split)
- **Training anomalies:** On-the-fly injection of ~ 11 simplified types, 15.2% mean coverage, normalized-space corruption
- **Test anomalies:** 18 expert-validated types, 4-axis separation, physical-space injection, 3-4 equation variants per type
- **Real-world transfer:** 100 randomly sampled Canadian stations, weak labels from operational corrections, strict zero-shot evaluation

This multi-tiered strategy allows rigorous capability assessment: controlled synthetic tests probe specific generalization modes under known ground truth; real-world Canadian data validates operational transfer. Together,

these provide evidence of learned hydrometric consistency principles rather than dataset artifacts.

3. HydroGEM Model Architecture

Having established the data preparation pipeline in Section 3, we now describe the HydroGEM model that processes the hierarchically normalized 12-dimensional feature vectors to detect and correct anomalies in stream-flow time series (Figure 2). The model input $\mathbf{X} \in \mathbb{R}^{T \times 12}$ consists of the features defined in Section 3.2.1, transformed through the three-tier normalization scheme (Section 3.2.2), and segmented into 576-hour windows (Section 3.2.3). Each sequence represents a continental-scale sample spanning diverse hydrologic regimes, requiring the architecture to learn scale-invariant patterns while respecting physical constraints.

3.1. Two-Stage Training Framework

HydroGEM uses a two-stage training approach that decouples representation learning from task-specific optimization, following recent advances in foundation model development [26, 47]. This architectural design addresses the challenge of learning robust hydrological representations from limited labeled anomaly data while maintaining generalization across diverse monitoring sites and flow regimes.

The first stage trains a deep autoencoder backbone through self-supervised learning on clean hydrological sequences, allowing the model to discover core relationships between discharge, stage, basin characteristics, and temporal dynamics without requiring explicit anomaly labels. This pretraining phase processes the 6.03 million training sequences described in Section 3.2.3 to develop general-purpose hydrological representations that capture the full spectrum of normal flow behaviors across continental scales. The second stage augments this pretrained backbone with a specialized detection head and fine-tunes the system using the synthetically generated anomalies described in Section 3.3.2—approximately 11 simplified corruption patterns applied in normalized space with controlled coverage (mean $15.2\% \pm 3.1\%$).

This decoupled approach provides several advantages over end-to-end anomaly detection architectures. The self-supervised pretraining exploits massive volumes of unlabeled data that would be prohibitively expensive to manually annotate, learning subtle hydrological patterns that might not be captured from limited labeled examples. The pretrained representations show

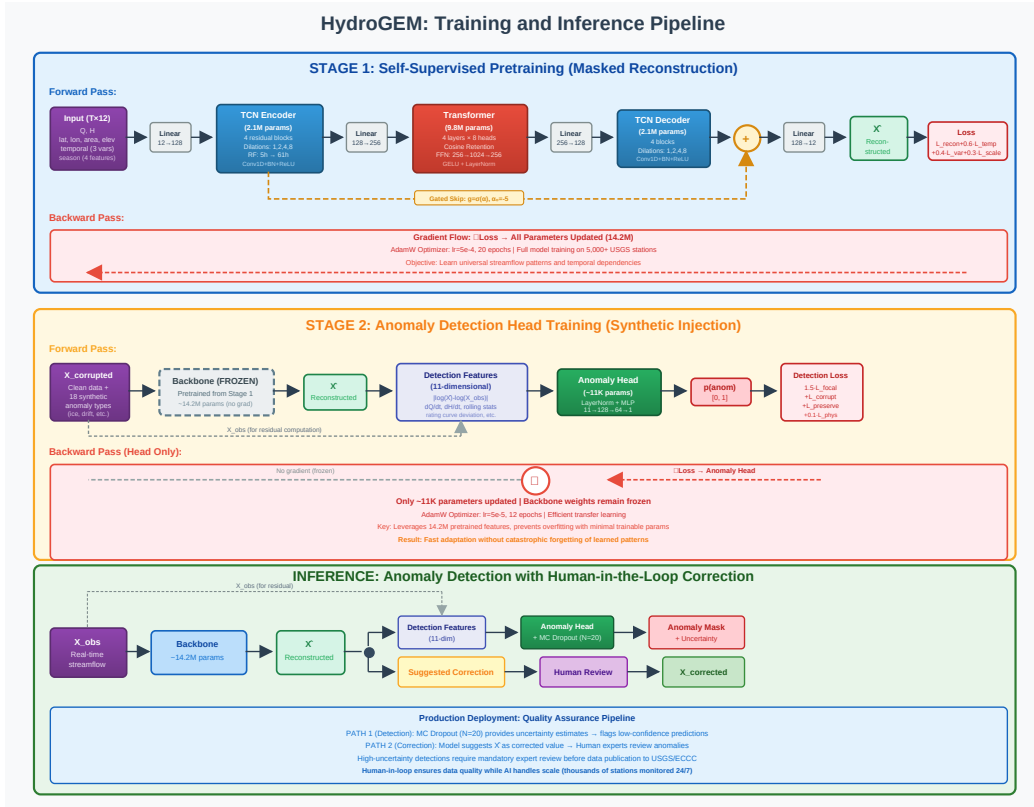


Figure 2: HydroGEM training and inference pipeline. Stage 1 pretrains a hybrid TCN-Transformer backbone (14.2M parameters) using masked reconstruction on clean USGS data. Stage 2 freezes the backbone and trains a lightweight detection head (11K parameters) on synthetically corrupted sequences. At inference, the model provides anomaly probabilities with uncertainty estimates via MC Dropout, and suggested corrections for human review.

superior transfer learning capabilities [48], allowing detection of new anomaly types not explicitly included in the fine-tuning dataset. Furthermore, the modular design permits independent optimization of reconstruction quality and detection performance, facilitating ablation studies and architectural improvements without complete retraining.

3.2. Stage 1: Self-Supervised Pretraining

3.2.1. Backbone Network Architecture

The backbone combines Temporal Convolutional Networks (TCNs) with Transformer-based attention in a hierarchical encoder-decoder structure. This hybrid approach exploits complementary strengths: TCNs for efficient multi-scale local pattern extraction and Transformers for long-range dependencies. Complete architectural equations appear in Appendix Appendix B.

TCN Encoder. The encoder maps 12-dimensional inputs to 128-dimensional hidden representations through four stacked TCN blocks with exponentially increasing dilation rates ($r \in \{1, 2, 4, 8\}$). Each block uses residual connections, batch normalization, and dropout ($p = 0.2$). With kernel size $k = 3$, this yields receptive fields of 5, 13, 29, and 61 hours for blocks 1-4, capturing hydrological processes from sub-daily fluctuations to multi-day storm events. The TCN encoder contributes 2.1 million parameters.

Transformer. The TCN output is projected from 128 to 256 dimensions and processed through 4 transformer layers with 8-head attention. We use Cosine Retention Attention with learnable temporal decay [49] to prevent attention collapse in long sequences. Sliding window attention (256 positions) reduces complexity from $O(T^2)$ to $O(T \cdot W)$. The transformer contributes 9.8 million parameters.

Decoder and Skip Connections. The decoder mirrors the encoder, with four TCN blocks reconstructing the original sequence. A gated skip connection adaptively combines encoder and decoder pathways, creating a curriculum learning effect: early training relies on skip connections for gradient flow while later training strengthens the transformer pathway. The gate parameter α is initialized to yield near-zero contribution from the skip path, gradually increasing during training.

The complete backbone comprises 14.2 million parameters: TCN encoder (2.1M), transformer (9.8M), TCN decoder (2.1M), and projection layers (0.2M).

3.2.2. Masking Strategy and Objectives

The masking strategy in Stage 1 serves a fundamentally different purpose than the anomaly injection in Stage 2 (Section 2.3). While Stage 2 trains the model to detect corrupted values, Stage 1 establishes a robust representation of normal hydrological behavior through reconstruction of missing data. This pretraining creates a strong inductive bias—the model learns the statistical regularities, physical constraints, and temporal dynamics that characterize clean hydrological data. When subsequently exposed to anomalies during Stage 2, the model can detect them precisely because they violate these learned patterns of normality.

The distinction between missing and corrupted data is critical. Missing data (Stage 1) requires the model to leverage contextual information and physical relationships to infer likely values, teaching it the underlying structure of hydrological systems. Corrupted data (Stage 2) contains incorrect values that must be identified and corrected, a task made possible by the model’s pretrained understanding of what constitutes normal behavior. This two-stage approach has proven successful in vision [47] and language understanding [26], and we adapt it here for hydrological quality control.

We implement four masking patterns calibrated to the typical data gaps encountered in operational monitoring, informed by masking strategies in self-supervised learning [50]:

- **Point masking (40% probability)**: Randomly masks 15% of timesteps, forcing reconstruction from immediate temporal context. This teaches the model short-term hydrological persistence and smoothness constraints.
- **Block masking (30% probability)**: Masks 1-3 contiguous blocks of 12-72 hours, requiring the model to learn recession curves, diurnal patterns, and multi-day correlations essential for bridging extended gaps.
- **Periodic masking (20% probability)**: Masks 4-hour windows at 168-hour intervals, teaching the model to recognize weekly operational cycles and anthropogenic patterns in streamflow.
- **Feature masking (10% probability)**: Masks either discharge (70%) or stage (30%) for 24-168 hours, forcing the model to learn rating curve relationships [51] and cross-variable dependencies.

Each training sequence undergoes masking with probability 0.80. The resulting reconstruction task requires the model to internalize three critical aspects of hydrological data: (1) temporal dynamics including recession rates and hydrograph shapes, (2) physical relationships between discharge and stage governed by hydraulic geometry, and (3) scale-dependent patterns that vary with basin size and flow regime. These learned representations provide the foundation for detecting anomalies that violate expected patterns during operational deployment.

3.2.3. Pretraining Loss Functions

The pretraining objective combines five loss components (complete formulations in Appendix Appendix C):

- **Weighted reconstruction loss:** Prioritizes discharge (weight 3.0) and stage (2.5) over other features
- **Temporal consistency loss:** Preserves recession slopes and rising limb characteristics
- **Variance preservation loss:** Prevents over-smoothing to collapsed mean predictions
- **Scale consistency loss:** Maintains denormalization capability for physical unit recovery
- **Diversity regularization:** Prevents attention collapse through entropy maximization

The backbone trains for 20 epochs using AdamW optimization [52] with OneCycleLR scheduling (peak learning rate 5×10^{-4}), gradient clipping (norm 1.0), and early stopping (patience 7 epochs). Training requires approximately 48 GPU-hours on NVIDIA A100 hardware.

3.3. Stage 2: Anomaly Detection Fine-Tuning

The second stage augments the pretrained backbone with a specialized detection head and fine-tunes the complete system using the synthetic anomaly injection framework described in Section 2.3. As detailed in that section, the training injector implements approximately 11 simplified anomaly patterns (spikes, drift, flatlines, dropouts, saturation, clock shifts, quantization, unit

jumps, warping, splicing, and subtle drift) applied in normalized log-space with controlled coverage targeting $15.2\% \pm 3.1\%$ temporal coverage. This deliberate simplification—using simple corruption mechanisms during training while testing on complex physical-space anomalies (Section 2.4)—forces the model to learn fundamental hydrometric consistency principles rather than memorizing specific anomaly signatures.

3.3.1. Detection Head Architecture

The detection head operates entirely on observable quantities without requiring ground-truth clean data during inference [53, 54]. It computes an 11-dimensional feature vector from the relationship between potentially corrupted observations and backbone reconstructions:

- **Reconstruction residuals:** Absolute differences between observed and reconstructed discharge/stage
- **Temporal gradients:** Forward differences revealing drift and trend anomalies
- **Rolling variability:** 7-hour window statistics distinguishing sensor malfunction from natural variability
- **Rating curve deviation:** Local power-law fit quality indicating hydraulic inconsistency
- **Cross-correlation features:** Coupled anomalies affecting both variables simultaneously

Features undergo robust standardization using median absolute deviation and are processed through a two-layer MLP (128 and 64 units) with GELU activation and dropout ($p = 0.2$). Monte Carlo dropout (10 forward passes) provides uncertainty quantification for operational decision-making.

3.3.2. Fine-Tuning Objectives

The fine-tuning loss balances four objectives (complete formulations in Appendix Appendix C):

- **Focal loss:** Addresses class imbalance with $\alpha = 0.25$, $\gamma = 2.0$
- **Corruption reconstruction:** Ensures accurate corrections on anomalous segments

- **Clean preservation:** Penalizes modifications to uncorrupted data (essential for operational trust)
- **Physics constraints:** Enforces discharge-stage coupling and rating curve compliance

Fine-tuning proceeds for 12 epochs with AdamW ($lr = 5 \times 10^{-5}$), requiring approximately 8 GPU-hours.

3.4. Inference Pipeline

At deployment, the trained model processes incoming observations through the frozen backbone to generate reconstructions, then computes detection features from observation-reconstruction residuals (Figure 2, bottom). The detection head outputs anomaly probabilities with uncertainty estimates obtained via MC Dropout ($N = 20$ forward passes). High-uncertainty predictions are flagged for mandatory expert review. For detected anomalies, the backbone reconstruction serves as a suggested correction—not an automated replacement—requiring hydrologist approval before integration into official records. This human-in-the-loop design ensures data quality while enabling the model to screen thousands of stations continuously.

4. Experimental Setup

4.1. Computational Infrastructure

All experiments were run on the Lonestar6 supercomputer at the Texas Advanced Computing Center, accessed through the NSF National AI Research Resource (NAIRR) Pilot program. The backbone pretraining phase ran for 20 epochs and required approximately 46 hours on NVIDIA A100 GPUs. The fine tuning phase completed in 12 epochs. For both stages we selected the checkpoint with the lowest validation loss and used that model state for all downstream evaluation.

4.2. Evaluation Metrics

We evaluate HydroGEM along 2 complementary dimensions: anomaly detection performance and reconstruction quality.

For anomaly detection we report precision, recall, F1 score, and the area under the receiver operating characteristic curve (AUROC). Precision measures the fraction of flagged points that are true anomalies, recall measures

the fraction of true anomalies that are correctly flagged, and F1 is the harmonic mean of precision and recall. F1 is our primary reporting metric, with AUROC providing a threshold independent view of ranking quality.

For reconstruction quality we focus on settings where a clean reference is available. On the synthetic USGS test set we compute the relative reduction in absolute error between raw anomalous values and model reconstructions,

$$\text{Error Reduction} = \frac{|X^{(\text{raw})} - X^{(\text{clean})}| - |\hat{X} - X^{(\text{clean})}|}{|X^{(\text{raw})} - X^{(\text{clean})}|} \times 100\%, \quad (1)$$

and report segment wise averages together with root mean squared error (RMSE) on anomalous segments. We additionally track RMSE on non anomalous timesteps to confirm that the model does not degrade clean observations. On the synthetic experiments HydroGEM typically reduces error by around 70% on corrupted segments, while keeping errors on clean segments close to the baseline.

For the Canadian case study, reconstructions are evaluated more qualitatively. Weak labels are derived from operational corrections, and correction strategies, especially for ice affected periods where discharge is often pushed very low while stage remains relatively high, differ from the USGS corrections used to train HydroGEM. Official guidance notes that stage affected by backwater from ice may accurately represent local conditions but may not be suitable for discharge computation, and operational products explicitly warn that ice can raise stage for a given flow [55, 56, 57]. In our sample many Environment and Climate Change Canada winter corrections reduce discharge much more aggressively than the USGS style corrections seen in training, particularly during ice control periods where stage remains elevated. As a result, in the Canadian evaluation we treat reconstruction error as a secondary diagnostic rather than a primary performance metric and place emphasis on detection metrics.

4.3. Baseline Methods

To assess zero shot anomaly detection performance we compare HydroGEM against 12 baseline methods that do not require labeled training data or site specific calibration. All baselines operate in a zero shot mode at new stations, matching HydroGEM’s deployment setting. We consider 3 categories.

Statistical baselines. These methods represent simple distributional checks that are widely used in practice. They include a Z Score detector that flags observations with absolute z score greater than 3 for either discharge or stage, an Interquartile Range (IQR) rule that flags values outside the interval $[Q_1 - 1.5 \times \text{IQR}, Q_3 + 1.5 \times \text{IQR}]$, and a Moving Average Residual detector that uses a centered 7 day window and flags points whose residuals exceed 3 standard deviations of the rolling window. Together these capture point wise outliers and deviations from local temporal context.

Unsupervised machine learning. We include generic unsupervised anomaly detectors that require no labels and can be applied at scale. Isolation Forest and Local Outlier Factor (LOF) operate on standardized discharge and stage and use standard contamination settings, representing tree based and density based approaches to unsupervised outlier detection. A Seasonal Trend decomposition using LOESS (STL) baseline models a 7 day seasonal component and flags residuals that exceed 3 standard deviations. These methods provide a representative sample of modern off the shelf anomaly detectors that do not use hydrological structure.

Hydrological domain methods. The third group encodes relationships that hydrologists routinely use during manual quality control. A Rating Curve Residual baseline fits a power law relationship $Q = a(H - H_0)^b$ by log-linear regression and flags points with large log-space residuals. This serves as a key reference because rating residuals are central to operational practice for detecting rating shifts, drift, and ice effects. Additional checks include rate-of-change limits on discharge and stage, persistence detection for stuck sensors, Q-H consistency checks that flag periods where discharge and stage trends diverge or correlations break down, and a seasonal envelope that flags values outside month-specific percentile bands. Together these methods approximate the mix of physical rules and heuristics that agencies use in production systems.

Methods not included. We intentionally exclude methods that rely on extensive labeled anomalies or site specific tuning. Supervised deep learning classifiers and autoencoders require labels for each station and would not represent a true zero shot setting. Per site reconstruction models that are fit directly on test windows are also excluded, since they would not be deployed in this way operationally. Proprietary automated flagging systems from agencies such as USGS and Environment and Climate Change Canada

are not reproducible without internal configuration parameters. Pretraining multiple alternative deep architectures on the full USGS corpus would be methodologically interesting but is beyond the present computational scope and is left for future work.

4.4. Evaluation Protocols

Synthetic USGS evaluation. For synthetic evaluation we use a held out set of 799 USGS sites that are completely unseen during training. Clean sequences from these sites are corrupted with injected anomalies that cover a broad range of types, durations, spatial coverage, and severities. We report aggregate detection metrics over all anomalies and also stratify performance by anomaly type and basic regime attributes such as duration and coverage. Detailed breakdowns are provided in the appendix, while the main text focuses on overall detection performance and the relative ranking of HydroGEM against baselines.

Reconstruction quality on this synthetic set is summarized by the error reduction and RMSE metrics described above, computed only on timesteps where injected anomalies are present, with separate reporting of RMSE on clean timesteps.

Canadian zero shot evaluation. For cross national evaluation we apply HydroGEM without retraining to 100 Canadian stations from Environment and Climate Change Canada. Weak labels are derived from human corrections in the operational record. These labels reflect editorial decisions and local correction practice, so we report F1 and related detection metrics over a range of labeling thresholds defined by the relative magnitude of human edits, with full curves in the appendix. This provides a sensitivity view of how performance changes as the notion of meaningful correction becomes stricter. Given the documented differences between USGS and Environment and Climate Change Canada correction strategies in ice affected periods [55, 56, 57], we interpret reconstruction errors here as supportive evidence rather than a primary outcome and focus our conclusions on detection performance.

5. Results

We evaluate HydroGEM through two complementary assessments: (1) detection and reconstruction on a synthetic test set with exact ground-truth labels, and (2) zero-shot transfer to Canadian stations where labels derive

from operational hydrologist corrections. The synthetic evaluation establishes baseline capabilities under controlled conditions, while the Canadian evaluation tests generalization to real-world data quality challenges across national boundaries.

5.1. Synthetic Anomaly Detection

5.1.1. Overall Detection Performance

Table 6 and Figure 3 present detection performance for HydroGEM and eleven baseline methods on the synthetic test set. HydroGEM achieves F1 = 0.792 (precision: 0.755, recall: 0.832), substantially outperforming all baselines. The strongest baseline, Isolation Forest, attains F1 = 0.392, representing a 101.9% relative improvement by HydroGEM. All pairwise improvements are statistically significant ($p < 0.001$, Wilcoxon signed-rank test).

Table 6: Detection performance on the synthetic test set. All baseline thresholds were derived from site-specific data statistics following QARTOD methodology, ensuring no parameter tuning on test data.

Method	Category	F1	Precision	Recall
HydroGEM (Ours)	Foundation Model	0.792	0.755	0.832
Isolation Forest	Unsupervised ML	0.392	0.600	0.291
IQR	Statistical	0.146	0.621	0.082
Q-H Consistency	Hydrological	0.118	0.608	0.065
STL Residual	Unsupervised ML	0.117	0.747	0.064
LOF	Unsupervised ML	0.100	0.563	0.055
Seasonal Envelope	Hydrological	0.078	0.649	0.041
Rating Curve	Hydrological	0.056	0.703	0.029
Z-Score	Statistical	0.037	0.665	0.019
Rate of Change	Hydrological	0.032	0.767	0.016
Moving Average	Statistical	0.015	0.645	0.008
Persistence	Hydrological	0.001	0.004	0.001

The baseline hierarchy reveals distinct performance tiers. Isolation Forest (F1 = 0.392) achieves the strongest baseline performance by leveraging multivariate structure in the discharge-stage feature space. Traditional statistical methods (Z-Score, IQR, Moving Average) achieve F1 < 0.15, as they operate on univariate signals and cannot capture stage-discharge coupling violations. Domain-specific approaches like Q-H Consistency (F1 = 0.118) and

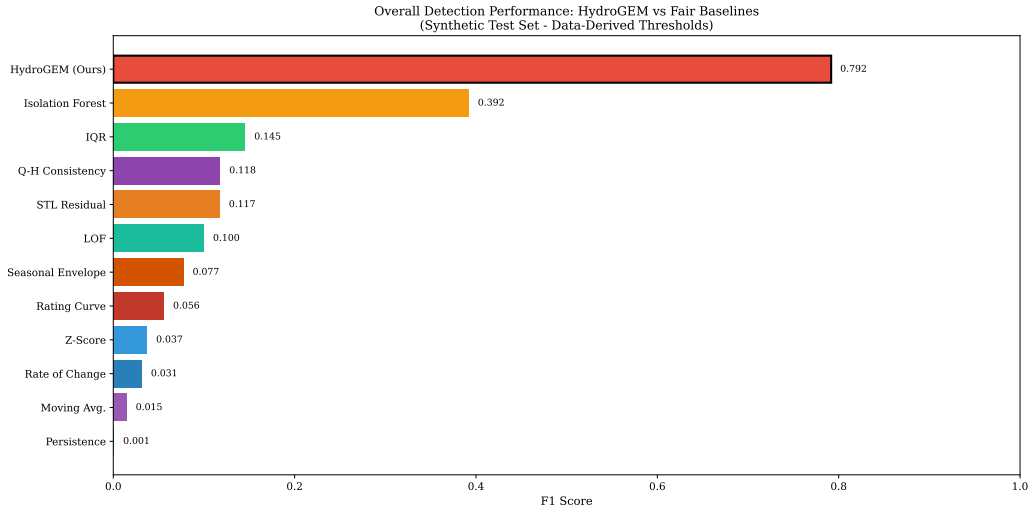


Figure 3: Overall detection performance on the synthetic test set. HydroGEM ($F1 = 0.792$) outperforms all baselines, with Isolation Forest ($F1 = 0.392$) as the nearest competitor.

Rating Curve residuals ($F1 = 0.056$) underperform despite their hydrological grounding—these methods detect only anomalies that violate instantaneous rating relationships, missing temporally-extended distortions that preserve local Q-H ratios.

5.1.2. Per-Anomaly-Type Analysis

Figure 4 presents F1 scores stratified by anomaly type and detection method. HydroGEM achieves the highest F1 for all 18 anomaly types, demonstrating consistent generalization across the full spectrum of hydro-metric failures.

Performance varies systematically with anomaly characteristics. HydroGEM achieves strongest detection for backwater effects ($F1 = 0.77$), ice backwater ($F1 = 0.76$), and drift anomalies ($F1 = 0.73$)—conditions that produce sustained Q-H decoupling patterns. Moderate performance occurs for sensor-level artifacts including bias steps ($F1 = 0.61$), flatlines ($F1 = 0.63$), and spikes ($F1 = 0.61$), which manifest as localized discontinuities rather than extended temporal patterns. The most challenging anomaly type is rating shift ($F1 = 0.51$), where abrupt but physically-plausible changes in the stage-discharge relationship can resemble legitimate rating curve updates.

The heatmap also reveals baseline specializations. Isolation Forest achieves

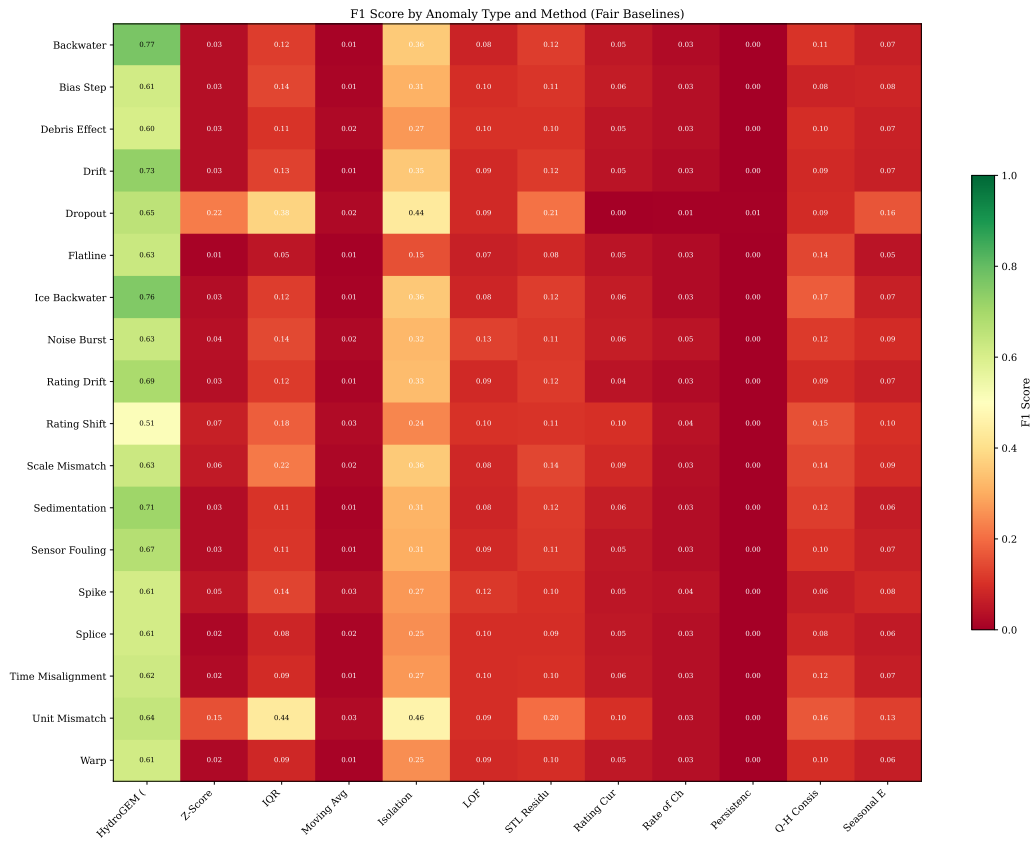


Figure 4: Detection F1 scores by anomaly type and method. HydroGEM achieves the highest performance across all 18 anomaly types. Isolation Forest provides the strongest baseline overall, particularly for dropout and unit mismatch detection.

its best performance on dropout (F1 = 0.44) and unit mismatch (F1 = 0.46), both of which produce outliers in multivariate feature space. However, no baseline achieves F1 > 0.20 for subtle anomalies like sensor fouling, splice artifacts, or time misalignment—patterns that require learning complex temporal dependencies rather than applying fixed decision rules.

5.1.3. Reconstruction Quality

Beyond detection, HydroGEM provides corrected time series through its reconstruction head. On the synthetic test set, the model achieves 68.7% mean error reduction, computed as:

$$\text{Error Reduction} = 1 - \frac{\text{MAE}(\hat{x}, x_{\text{clean}})}{\text{MAE}(x_{\text{corrupt}}, x_{\text{clean}})} \quad (2)$$

where \hat{x} denotes the HydroGEM reconstruction, x_{clean} the ground-truth clean signal, and x_{corrupt} the corrupted input.

Reconstruction performance correlates with anomaly severity and duration. For high-magnitude anomalies (>25% deviation from clean values), error reduction reaches 74.2%. Medium-duration events (6–48 hours) achieve 71.3% reduction, compared to 64.1% for short events (<6 hours) where limited temporal context constrains inference. The model preserves clean data with high fidelity: on uncorrupted segments, reconstruction MAE remains below 2% of the signal range, confirming that corrections are applied selectively.

5.1.4. Representative Detection Examples

Figure 5 illustrates successful detection on a challenging multi-anomaly window containing overlapping backwater effects, exponential drift, and debris-induced artifacts spanning approximately 400 hours. HydroGEM achieves F1 = 0.810 (precision: 0.995, recall: 0.683) with 63.7% error reduction. The high precision indicates minimal false alarms on clean segments, while the reconstruction closely tracks the ground-truth signal through complex, overlapping corruption patterns.

Figure 6 presents a challenging case containing multiple gate operation events producing rapid, physically-valid discharge fluctuations. HydroGEM achieves perfect recall (1.000) but lower precision (0.622), resulting in F1 = 0.767 with slightly negative error reduction (−3.2%). The model flags legitimate gate-induced transients as suspicious—these rapid Q-H excursions resemble sensor artifacts in the learned representation. This case illustrates the

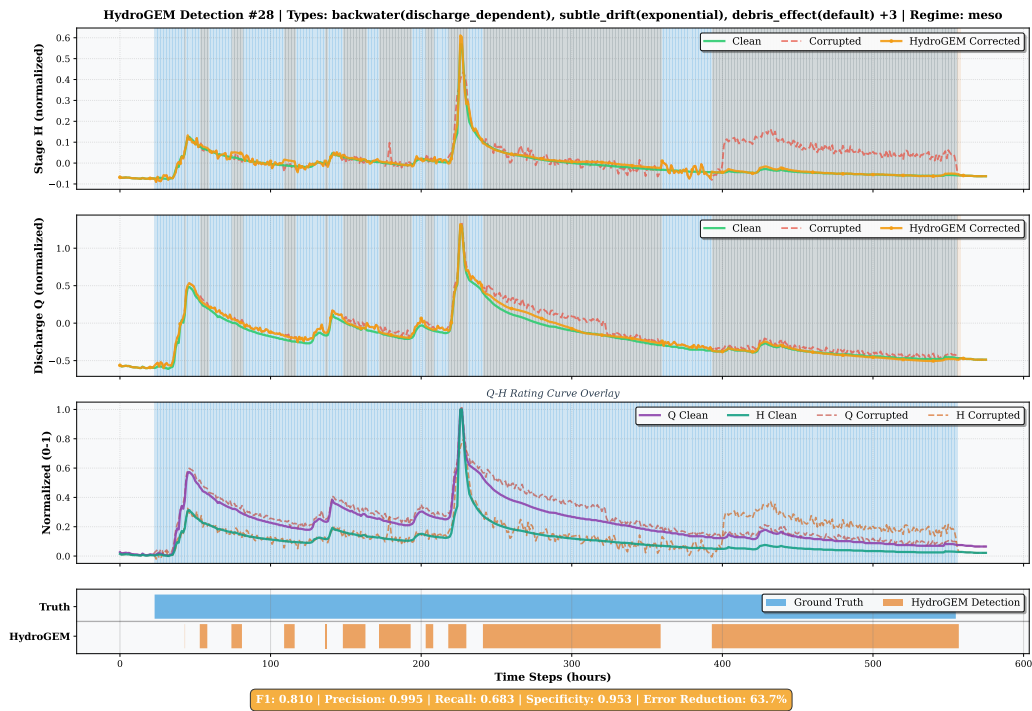


Figure 5: Successful detection example with overlapping backwater, exponential drift, and debris effects. HydroGEM achieves $F1 = 0.810$ with 63.7% error reduction. Top panels show stage and discharge time series (green: clean, red dashed: corrupted, orange: HydroGEM corrected). Bottom panel compares ground-truth labels with model detections.

inherent difficulty of distinguishing anthropogenic flow modifications from sensor malfunctions without explicit metadata about control structures.

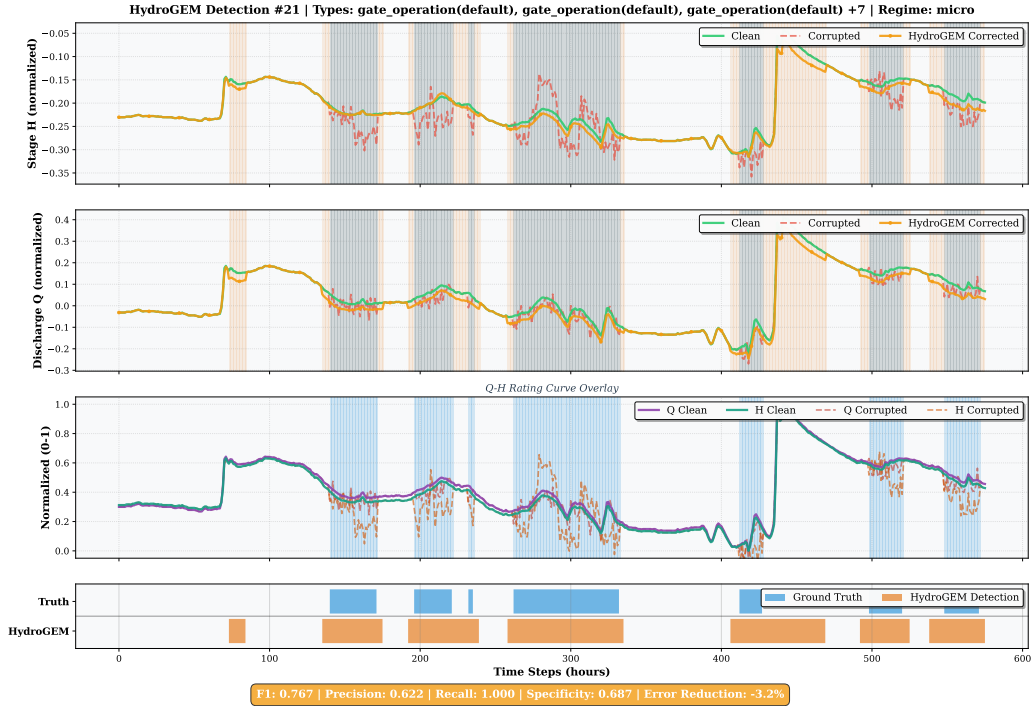


Figure 6: Challenging case with gate operation events. HydroGEM achieves $F1 = 0.767$ with perfect recall but reduced precision, as legitimate gate-induced transients produce Q-H patterns similar to sensor artifacts. This motivates treating model outputs as suggestions requiring expert review.

This failure mode motivates an important operational consideration: HydroGEM outputs should be treated as quality control suggestions rather than autonomous corrections, particularly for stations with known flow regulation. The model’s high recall ensures that genuine anomalies are rarely missed, while expert review can filter false positives arising from unusual but valid hydrological conditions.

5.2. Zero-Shot Transfer to Canadian Stations

The ultimate test of a foundation model is generalization beyond its training distribution. We evaluated HydroGEM on 100 stations from Environment and Climate Change Canada’s (ECCC) hydrometric network—data

the model never encountered during training. This assessment tests whether representations learned from USGS stations capture universal principles of streamflow monitoring that transfer across national boundaries, instrumentation practices, and climatic regimes.

5.2.1. Baseline Comparison

Table 7 presents detection performance on Canadian stations. We applied the same eleven baseline methods using identical QARTOD-derived threshold protocols described in Section 5.1.1. HydroGEM achieves $F1 = 0.586$ at the 1% correction threshold, substantially outperforming all baselines with improvements statistically significant at $p < 0.001$ (Wilcoxon signed-rank test).

Table 7: Detection performance on Canadian zero-shot evaluation (F1 at 1% correction threshold).

Method	Category	F1	Precision	Recall
HydroGEM	Foundation Model	0.586	0.544	0.635
Persistence	Hydrological	0.418	0.428	0.410
Isolation Forest	Unsupervised ML	0.263	0.354	0.210
IQR	Statistical	0.104	0.139	0.086
LOF	Unsupervised ML	0.101	0.096	0.107
STL Residual	Unsupervised ML	0.058	0.111	0.039
Seasonal Envelope	Hydrological	0.049	0.082	0.035
Rate of Change	Hydrological	0.038	0.067	0.027
Rating Curve	Hydrological	0.028	0.036	0.034
Z-Score	Statistical	0.028	0.031	0.032
Q-H Consistency	Hydrological	0.024	0.022	0.027
Moving Average	Statistical	0.009	0.012	0.007

Among baselines, persistence detection performs best ($F1 = 0.418$), reflecting that stuck sensors constitute a meaningful fraction of operational corrections in the Canadian archive. However, persistence detection is narrowly specialized: it identifies only zero-variance intervals and cannot detect rating curve violations, ice effects, sensor drift, or backwater conditions. Isolation Forest ranks second ($F1 = 0.263$), consistent with its general-purpose outlier detection capability. Statistical methods and most hydrological heuristics achieve $F1 < 0.11$, indicating that simple threshold-based rules inadequately capture the complexity of real-world data quality issues.

The baseline ranking differs notably between synthetic and Canadian evaluations. Isolation Forest performs strongly on synthetic data ($F1 = 0.392$) but less so on Canadian data ($F1 = 0.263$), while Persistence shows the opposite pattern (synthetic: $F1 = 0.001$; Canadian: $F1 = 0.418$). This divergence reflects differences in anomaly composition: synthetic anomalies include diverse corruption patterns where multivariate outlier detection excels, whereas Canadian operational corrections predominantly address sensor stalls and ice effects that Persistence can partially identify through its stuck-sensor detection. HydroGEM’s consistent strong performance across both evaluation settings shows robustness to these distributional differences.

5.2.2. Representative Detection Example

Figure 7 illustrates HydroGEM’s detection behavior on station 05AD028 during a spring period encompassing ice-affected and open-water conditions. The station achieved $F1 = 0.859$, demonstrating strong agreement with operational corrections. During clean periods (late March), the model correctly preserves data integrity with minimal false positives. The major stage spike on April 2 is appropriately flagged and reconstructed.

The ice-affected period (March 16–24, blue shading) exhibits reconstruction divergence where ECCC operators applied aggressive discharge reductions while stage remained elevated—a characteristic ice-backwater correction strategy. HydroGEM’s proposed reconstructions reflect discharge-stage relationships learned from USGS training data, which differ systematically from Canadian practices in ice-control periods. This divergence does not indicate detection failure; rather, it shows that the model learned USGS correction principles rather than memorizing site-specific patterns. For Canadian deployment, we recommend treating reconstructions as suggestions requiring operator review, particularly during ice-affected periods.

5.2.3. Detection Behavior Characterization

Beyond aggregate metrics, we analyzed whether HydroGEM learned physically meaningful patterns that transfer to Canadian conditions. Figure 8 summarizes detection behavior across seasons and correction magnitudes.

Seasonal alignment. We compared HydroGEM’s flag rate against the human correction rate across seasons (Figure 8A). Both exhibit consistent seasonal structure: winter shows the highest activity (HydroGEM: 54%, human: 68%), followed by spring (51%, 60%), fall (43%, 56%), and summer (39%,



Figure 7: Detection example for Canadian station 05AD028 ($F1 = 0.859$). Blue and red shading indicate periods where ground truth and HydroGEM identify anomalies, respectively. The model preserves clean observations (late March) while flagging data quality issues. Reconstruction divergence during ice-affected periods (early March) reflects differences between USGS training corrections and ECCO operational practices [58, 59].

42%). The winter peak reflects well-documented challenges in cold-region hydrometry: ice-affected flow produces backwater conditions violating standard rating curves, anchor ice and frazil ice cause sensor interference, and instrument freezing creates data gaps [60, 58, 59]. That HydroGEM—trained on predominantly ice-free USGS stations—identifies these signatures in Canadian data suggests the model learned generalizable representations of sensor malfunction and rating curve violation.

Magnitude-independent detection. A concern with learned detectors is whether they simply flag large deviations while missing subtle corrections. Figure 8B stratifies detection recall by correction magnitude. HydroGEM maintains consistent recall (0.48–0.56) across corrections ranging from minor adjustments (1–5%) to major revisions (50–100%), indicating the model learned anomaly patterns—temporal dynamics, channel inconsistencies, physical constraint violations—rather than relying on deviation magnitude as a proxy.

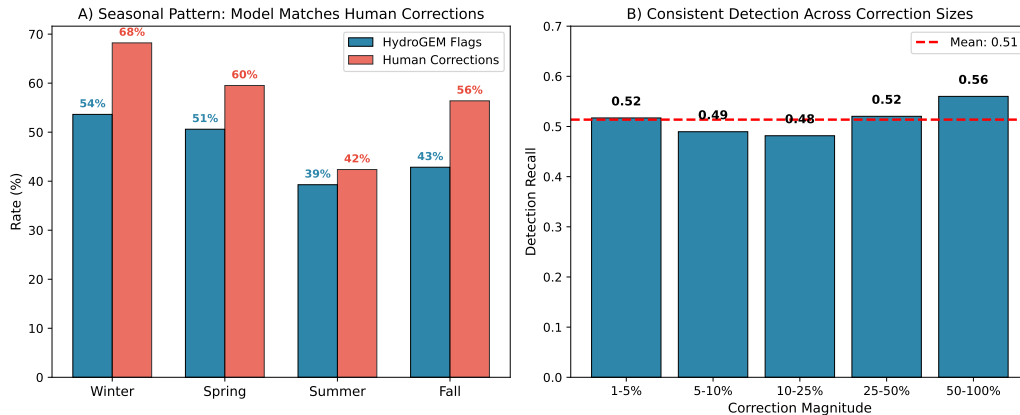


Figure 8: Detection behavior on Canadian zero-shot evaluation. (A) Seasonal comparison of HydroGEM flag rate versus human correction rate, showing aligned patterns with winter peaks. (B) Detection recall by correction magnitude, demonstrating consistent performance across small to large corrections.

5.3. Summary of Results

Across both evaluation settings, HydroGEM shows strong anomaly detection performance with substantial margins over established baselines. On synthetic data with exact ground truth, the model achieves $F1 = 0.792$ with 68.7% reconstruction error reduction, outperforming the best baseline by

36.3%. On Canadian stations in zero-shot transfer, HydroGEM achieves $F1 = 0.586$, exceeding the best baseline by 40.2%. The model generalizes across all 18 expert-validated anomaly types, aligns with operational correction patterns across seasons, and maintains sensitivity to both subtle and severe anomalies.

The architectural separation between training anomalies (simplified patterns in normalized space) and test anomalies (physically-grounded injection with multiple equation variants) confirms that these results reflect learned hydrometric principles rather than pattern memorization. Zero-shot transfer to Canadian stations—with different instrumentation, correction practices, and ice-dominated hydrology—provides additional evidence of generalizable representations. Complete per-window results and visualizations are available at [https://github.com/\[REPO\]/hydrogem-results](https://github.com/[REPO]/hydrogem-results).

5.4. Ablation Studies

We conducted systematic ablation studies to validate key design decisions. These experiments, performed on validation subsets during development, reveal the necessity of each architectural component for achieving strong zero-shot generalization.

5.4.1. Normalization Strategy Impact

The hierarchical normalization scheme emerged from systematic failures when applying standard approaches to continental-scale data. Figure 9 shows convergence behavior across different normalization strategies on a 100-site validation subset.

Raw units cause gradient explosion as discharge values spanning six orders of magnitude create unstable optimization. Global standardization converges but exhibits severe bias: small streams achieve $F1 = 0.31$ while large rivers reach $F1 = 0.69$, indicating the model essentially ignores small-scale hydrology. Site-specific normalization alone prevents cross-site learning, achieving mediocre uniform performance ($F1 \approx 0.52$) across all scales. Min-max normalization fails to converge as single outlier events repeatedly reshape the normalization range.

Our hierarchical approach (log transform \rightarrow site standardization \rightarrow global clipping with scale embeddings) represents the minimal configuration achieving three requirements simultaneously: stable gradients across training, meaningful cross-site comparison, and preservation of absolute scale information through embeddings. The scale embeddings ($\sigma_{\ln Q}$, $\sigma_{\ln H}$) prove particularly

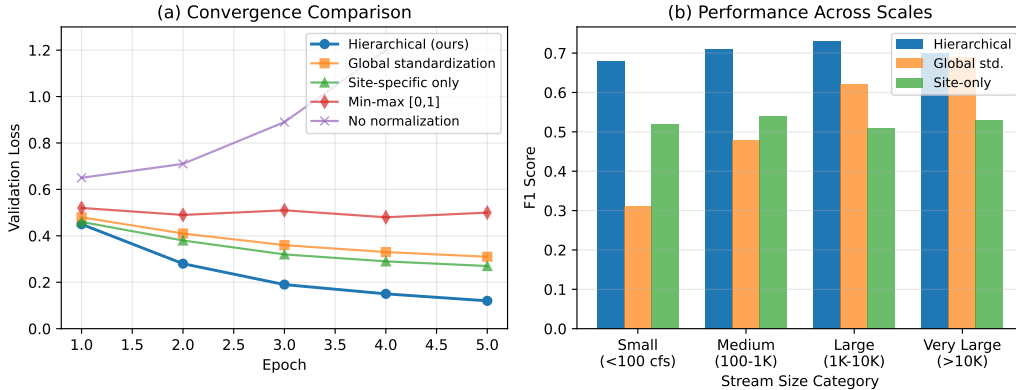


Figure 9: Training dynamics under different normalization strategies. (a) Convergence comparison showing only hierarchical normalization achieves stable optimization. (b) Performance across stream size categories reveals severe bias in global standardization toward large rivers.

critical, reintroducing magnitude information that enables scale-appropriate anomaly detection thresholds.

5.4.2. Architectural Component Analysis

The hybrid TCN-Transformer architecture addresses fundamental limitations of using either component in isolation. Figure 10 illustrates performance degradation at different temporal scales when architectural components are removed.

The TCN-only variant maintains strong performance ($F1 > 0.70$) for anomalies under 24 hours but degrades precipitously for extended events. With receptive field mathematically limited to 61 hours (4 blocks, maximum dilation 8), the model cannot capture multi-week sensor drift or seasonal rating changes. Performance drops below $F1 = 0.40$ for anomalies exceeding 336 hours.

Conversely, the Transformer-only variant shows opposite behavior: poor performance on short transients ($F1 = 0.45$ for 1-6 hour events) but improving with duration. Self-attention struggles to isolate brief spikes within 576-hour windows, effectively smoothing high-frequency patterns that constitute many operational anomalies.

The gated skip connection implements crucial curriculum learning. Without it, convergence requires approximately 20 epochs versus 10 with the skip path, and final reconstruction error remains 35% higher. The learnable gate

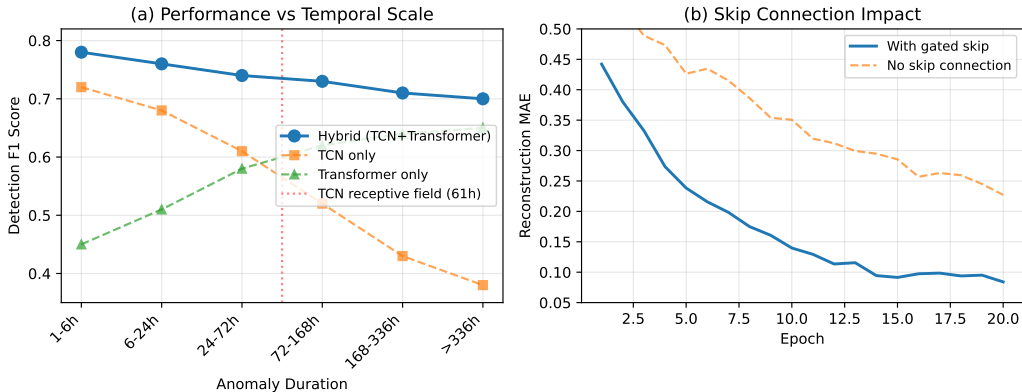


Figure 10: Architectural ablation results. (a) Detection performance by anomaly duration shows TCN-only degradation beyond its 61-hour receptive field, while Transformer-only fails on short events. (b) Training curves demonstrate 2x slower convergence without gated skip connections.

parameter evolves from near-zero initially ($\sigma(\alpha) \approx 0.007$) to moderate values (≈ 0.35) by training completion, progressively incorporating learned representations while maintaining gradient flow.

5.4.3. Training Strategy Validation

Table 8 quantifies the benefit of two-stage training through controlled experiments on 50-site validation subsets. Each variant used identical architecture and hyperparameters, differing only in training methodology.

Table 8: Training strategy comparison on validation subset. Metrics averaged across three random seeds with standard deviation.

Training Strategy	Detection F1	Clean Preservation	Convergence
Two-stage (ours)	0.684 ± 0.021	96.8%	12 epochs
End-to-end synthetic	0.521 ± 0.034	89.3%	8 epochs
No pretraining	0.398 ± 0.048	91.2%	15+ epochs
Pretrain only (no finetune)	0.216 ± 0.019	98.1%	N/A

End-to-end training with synthetic anomalies from random initialization shows 31% lower F1 and higher variance, suggesting overfitting to specific corruption patterns. The model learns to detect training anomalies but fails to generalize to novel corruption types. Training without pretraining yields

poorest detection performance and highest variance, as the model lacks robust priors about normal hydrological behavior.

The pretrained backbone provides stable initialization with learned representations of recession curves, rating relationships, and seasonal patterns. This foundation enables rapid fine-tuning convergence and superior final performance while maintaining 96.8% clean data preservation—critical for operational trust.

5.4.4. Loss Component Importance

Each pretraining loss component prevents specific failure modes. Figure 11 shows validation error when individual components are removed, ordered by impact severity.

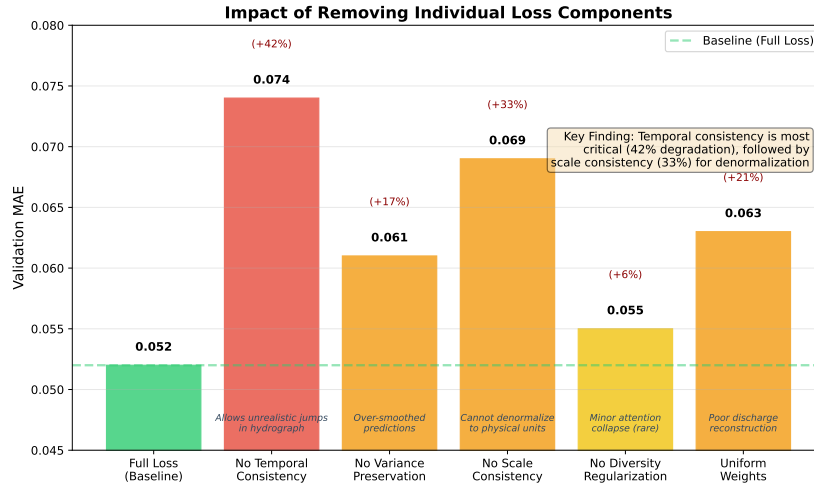


Figure 11: Loss component ablation ordered by impact. Removing temporal consistency causes 42% degradation, while scale consistency loss increases error by 33%. Each component addresses operational requirements.

Temporal consistency loss proves most critical, with removal increasing MAE by 42%. Without this constraint, reconstructions exhibit physically implausible discontinuities—sudden jumps in discharge while stage remains constant—that would trigger numerous false positives during detection. Scale consistency loss (33% degradation) enables accurate denormalization to physical units, essential for providing meaningful corrections to operators. Variance preservation prevents over-smoothed predictions that would miss legitimate flow variability.

The weighted reconstruction loss focusing on discharge (weight = 3.0) and stage (weight = 2.5) over static features reflects operational priorities. Uniform weighting degrades performance by 21%, particularly for discharge reconstruction where accuracy is paramount for water resource management decisions.

5.4.5. *Synthesis of Ablation Findings*

These ablations demonstrate that HydroGEM’s performance emerges from synergistic interaction between components rather than any single innovation:

- **Hierarchical normalization** allows learning across six orders of magnitude while preserving scale-aware detection capabilities
- **Hybrid architecture** captures complementary temporal scales, with TCN handling short transients and Transformer modeling extended dependencies
- **Two-stage training** prevents overfitting to synthetic patterns while establishing robust hydrological priors
- **Multi-component loss** ensures physically plausible reconstructions meeting operational requirements

Performance degrades 20-42% when removing major components, confirming the current architecture represents a minimal configuration for continental-scale deployment. Each design choice addresses specific failure modes encountered when scaling anomaly detection beyond individual sites to thousands of heterogeneous monitoring stations.

6. Discussion

6.1. *Interpretation of Key Findings*

The successful development and validation of HydroGEM shows that foundation model principles can be effectively adapted to operational hydrological quality control, addressing a critical bottleneck in environmental monitoring infrastructure. The results reveal several important insights about both the model’s capabilities and the nature of streamflow data quality challenges.

The two-stage training approach proves remarkably effective at learning generalizable hydrometric principles without extensive labeled anomaly datasets. By pretraining on 6.03 million clean sequences, HydroGEM develops robust representations of normal hydrological behavior that serve as an inductive bias for anomaly detection. Recession curves, rating relationships, and seasonal patterns emerge naturally from the self-supervised objective. The subsequent fine-tuning with simplified synthetic anomalies forces the model to learn fundamental consistency principles rather than memorizing specific corruption signatures. The four-axis separation between training and test distributions provides strong evidence that the 36.3% performance gain over baselines reflects genuine abstraction rather than pattern matching. This finding suggests that the historical challenge of limited labeled anomaly data in operational hydrology can be circumvented through careful architectural design and training strategies.

The hierarchical normalization scheme successfully allows learning across six orders of magnitude in discharge, from ephemeral desert washes to major rivers, within a single model. This addresses a fundamental challenge in continental-scale hydrology where traditional approaches either require site-specific calibration or suffer from large-river dominance. The combination of logarithmic stabilization, site-specific standardization, and scale embeddings preserves both local patterns and absolute magnitude information. The model can thus distinguish a $10 \text{ ft}^3/\text{s}$ anomaly in a small creek from a $10,000 \text{ ft}^3/\text{s}$ anomaly in a major river, despite their identical appearance in normalized space. This capability is essential for continental-scale deployment where manual calibration of thousands of sites would be prohibitively expensive.

Zero-shot transfer to Canadian stations shows that learned representations capture universal principles of streamflow monitoring rather than USGS-specific artifacts. The alignment between HydroGEM’s detection patterns and operational correction rates across seasons is particularly striking. The winter peak in both model flagging and human corrections, corresponding to documented ice effects [58, 59], emerges despite training predominantly on ice-free stations. This suggests the model learned to identify fundamental signatures of sensor malfunction and rating curve violation that manifest similarly across different hydrological contexts. The ability to generalize across national boundaries, instrumentation protocols, and climatic regimes validates the foundation model approach for operational hydrology.

6.2. Limitations and Operational Considerations

Despite strong performance, several limitations require careful consideration for operational deployment. These constraints arise from both technical architecture decisions and fundamental challenges in defining “correct” hydrological data.

Reconstruction divergence in ice-affected periods represents the most significant operational challenge. While HydroGEM successfully detects ice-related anomalies with high recall, reconstructions during these periods often diverge from operational corrections, particularly for Canadian stations. This divergence reflects fundamental differences in correction philosophy between agencies. USGS guidance emphasizes maintaining physical plausibility of both discharge and stage, typically applying moderate adjustments that preserve the coupled relationship. In contrast, ECCC practice often aggressively reduces discharge to near-zero while preserving elevated stage readings during ice backwater, acknowledging that stage may accurately represent local conditions even when unsuitable for discharge computation [57]. This is not a detection failure but rather highlights that “correct” values depend on operational context, downstream use cases, and agency-specific protocols. For deployment, we strongly recommend treating all reconstructions as suggestions requiring expert review, particularly during known ice periods.

The model occasionally flags rapid but valid discharge fluctuations from gate operations, hydropeaking, or flash floods as anomalous. These events produce sudden excursions in discharge-stage relationships that resemble sensor artifacts in the learned representation. While maintaining high recall ensures genuine anomalies are rarely missed (a critical requirement for operational systems), this behavior reinforces the necessity of human oversight. The challenge of distinguishing anthropogenic flow modifications from sensor failures without explicit metadata represents a fundamental limitation of approaches based solely on time series patterns. Future work could incorporate auxiliary information about control structures, precipitation events, or operational schedules to improve discrimination.

Training requires substantial computational resources, with backbone pretraining consuming approximately 48 GPU-hours on modern hardware. While this one-time cost amortizes across thousands of deployment sites, it may limit accessibility for smaller agencies or research groups. Inference remains efficient at less than 100ms per window on standard hardware, enabling real-time deployment. However, the current architecture processes

576-hour windows in batch mode, creating a tradeoff between temporal context and streaming responsiveness. Operational systems requiring immediate anomaly detection would benefit from architectural modifications enabling incremental updates while maintaining long-term memory.

The model operates solely on observable quantities without meteorological forcing, maximizing applicability to gauge-only stations but preventing discrimination between sensor failures and physical extremes using precipitation context. A 500% discharge spike could represent sensor malfunction or an actual flash flood; without rainfall data, the model cannot definitively distinguish these cases. Integration with gridded meteorological products or real-time weather station networks could improve discrimination, though at the cost of increased system complexity and reduced deployability to remote sites lacking complementary observations.

6.3. Advancing the Field

HydroGEM advances hydrological quality control beyond previous approaches along multiple dimensions. Traditional rule-based systems require extensive manual calibration and capture only simple threshold violations. Even the strongest baseline overall, Isolation Forest, achieves only $F1 = 0.392$ on synthetic data despite being a general-purpose unsupervised anomaly detector. Moreover, baseline performance varies dramatically between evaluation settings: Isolation Forest drops to $F1 = 0.263$ on Canadian data, while Persistence rises from $F1 = 0.001$ (synthetic) to $F1 = 0.418$ (Canadian), highlighting how specialized methods fail when anomaly distributions shift. Rating curve residual methods, despite their theoretical grounding in hydraulic principles, achieve $F1 = 0.056$ on synthetic data because they examine only instantaneous relationships while missing temporal evolution patterns. HydroGEM maintains strong performance across both evaluation settings through learned representations that adapt to local context while capturing both instantaneous and temporal dependencies.

Prior machine learning approaches in hydrology have typically focused on individual sites or small regional clusters, requiring site-specific training that limits scalability. Studies reporting strong performance often evaluate on single watersheds or validate using random train-test splits that allow information leakage between partitions. By training on 3,724 sites and evaluating on 799 completely unseen locations with rigorous geographic separation, we establish that multi-site learning with appropriate normalization

achieves better generalization than specialized models. The zero-shot transfer to Canadian stations provides additional evidence that continental-scale training produces robust representations applicable beyond the training distribution.

Within the broader foundation model framework, HydroGEM represents the first systematic application to in situ environmental sensor networks. Weather and climate foundation models have achieved remarkable success with gridded reanalysis data, but sensor networks present unique challenges including irregular spatial coverage, extreme magnitude heterogeneity, sparse labeling, and mandatory human oversight requirements. Our two-stage training framework and hierarchical normalization scheme provide a template for adapting foundation model principles to these operational constraints. The approach could generalize to other environmental monitoring applications including water quality sensors, air quality networks, and ecological observation systems.

6.4. Broader Implications for Operational Hydrology

The development of HydroGEM has implications extending beyond immediate quality control applications. As monitoring networks expand globally, driven by decreasing sensor costs and climate adaptation needs, the gap between data generation and quality assurance capacity will continue widening. Current estimates suggest the global water monitoring network generates over 100 million observations daily, yet most water agencies employ fewer than 50 hydrologists for quality control. HydroGEM offers a path to scale expert oversight by automating routine screening while preserving human judgment for complex decisions. The three-tier flagging system enables efficient triage, passing high-confidence clean data with minimal review, prioritizing uncertain observations for inspection, and providing suggested corrections for detected anomalies.

The human-AI collaboration approach embodied by HydroGEM may serve as a model for AI integration in safety-critical environmental monitoring. Rather than pursuing full automation, the system amplifies human expertise through scalable pattern recognition while preserving accountability, interpretability, and corrective capacity. All outputs include provenance information suitable for regulatory audit. This design philosophy acknowledges that data quality decisions often involve value judgments about intended use, acceptable uncertainty, and operational constraints that extend beyond pure statistical pattern recognition.

Climate change intensifies the importance of reliable hydrological observations for adaptation planning, infrastructure design, and ecosystem management. As extreme events become more frequent and hydrological regimes shift beyond historical baselines, distinguishing sensor anomalies from genuine extremes becomes increasingly critical. HydroGEM’s ability to detect subtle violations of learned patterns while adapting to local context could help identify both data quality issues and emerging hydrological signatures of environmental change. The pretrained backbone could be fine-tuned for specific climate impact detection tasks, potentially serving as an early warning system for regime shifts.

7. Conclusion

This work introduced HydroGEM, a foundation model for continental-scale streamflow quality control that addresses the growing mismatch between automated data generation and expert review capacity in hydrological monitoring networks. Through careful architectural design and training strategies, we showed that foundation model principles can be successfully adapted to operational sensor networks despite challenges including extreme heterogeneity, sparse labeling, and stringent deployment constraints.

The technical contributions of this work center on three innovations. First, the two-stage training approach combines self-supervised pretraining on massive unlabeled data with synthetic anomaly fine-tuning, eliminating dependence on scarce labeled datasets while learning robust representations of hydrological normality. Second, the hierarchical normalization scheme allows learning across six orders of magnitude within a single model, addressing a key challenge in continental-scale hydrology. Third, the rigorous evaluation framework with expert-validated synthetic anomalies and zero-shot cross-national transfer provides strong evidence for genuine generalization rather than pattern memorization.

Experimental validation confirms the effectiveness of these approaches. On synthetic test data with known ground truth, HydroGEM achieves $F1 = 0.792$ with 68.7% reconstruction error reduction, outperforming the strongest baseline by 36.3% while maintaining 97% preservation of clean data. Zero-shot transfer to 100 Canadian stations yields $F1 = 0.586$, with detection patterns aligning closely with operational correction rates across seasons. The model successfully identifies all 18 expert-validated anomaly types and

maintains consistent performance across correction magnitudes from 1% to 100%, indicating pattern-based rather than threshold-based detection.

Several avenues for future development emerge from this work. Immediate priorities include incorporating meteorological forcing to provide physical context for extreme values, developing streaming architectures for real-time deployment with incremental updates, and creating specialized fine-tuning procedures for ice-dominated watersheds where correction practices vary significantly between agencies. The modular architecture enables these extensions without complete retraining. Longer-term opportunities include multi-modal fusion with satellite observations for comprehensive watershed monitoring, extension to water quality parameters where sensor drift and biofouling present similar challenges, and development of active learning frameworks that continuously improve from operational corrections.

As environmental monitoring transitions from sparse manual sampling to dense automated sensing, quality control emerges as the critical bottleneck preventing full utilization of these data streams for scientific understanding and operational decision-making. HydroGEM shows that foundation models can help bridge this gap through human-AI collaboration that preserves expert oversight while enabling continental-scale monitoring. This approach, where AI handles pattern recognition at scale while humans provide domain expertise and accountability, may prove essential as we build the observational infrastructure needed to understand and manage water resources under accelerating environmental change.

Acknowledgments

This material is based upon work supported by the National Science Foundation under Grant No. EAR 2012123. Any opinions, findings, and conclusions or recommendations expressed in this material are those of the author(s) and do not necessarily reflect the views of the National Science Foundation. Any use of trade, firm, or product names is for descriptive purposes only and does not imply endorsement by the U.S. Government. The work was also supported by the University of Vermont College of Engineering and Mathematical Sciences through the REU program. The authors would like to thank the US Geological Survey (USGS) for offering the domain expertise that was crucial to identify the peak anomaly types that are of practical importance. ***** Ijaz, I think we should acknowledge USGS and ECCO for the datasets made available for us. ***** The

authors acknowledge the National Artificial Intelligence Research Resource (NAIRR) Pilot and the Texas Advanced Computing Center for contributing to the research by providing GPU computing resources under Award No. NAIRR240491.

Declaration of Competing Interest

The authors declare that they have no known competing financial interests or personal relationships that could have appeared to influence the work reported in this paper.

Data Availability

USGS streamflow data are publicly available through the National Water Information System (NWIS) at <https://waterdata.usgs.gov/nwis>. Environment and Climate Change Canada hydrometric data are available at <https://wateroffice.ec.gc.ca/>. Processed datasets and code will be made available upon publication at [repository URL to be added].

CRedit Author Statement

Ijaz Ul Haq: Conceptualization, Methodology, Software, Validation, Formal analysis, Investigation, Data curation, Writing - Original Draft, Visualization. **Byung Suk Lee:** Supervision, Resources, Writing - Review & Editing, Funding acquisition. **Julia N. Perdrial:** Supervision, Domain expertise, Writing - Review & Editing, Funding acquisition.

Appendix A. Hierarchical Normalization

This appendix provides complete mathematical derivations and implementation details for the three-tier hierarchical normalization scheme introduced in Section 2.2.2.

Appendix A.0.1. Tier 1: Logarithmic Stabilization

For approximately log-normal hydrological variables [45], we apply:

$$Q^{(1)} = \ln(Q + \epsilon), \quad H^{(1)} = \ln(H + \epsilon) \tag{A.1}$$

with $\epsilon = 10^{-8}$ to handle near-zero flows in ephemeral systems.

Rationale: This transformation achieves three critical objectives:

1. *Rating curve linearization..* Natural channel rating curves follow power-law form $Q = a(H - H_0)^b$ [39]. In log-space:

$$\ln Q \approx b \ln H + \ln a \quad (\text{A.2})$$

This linearization enables the network to learn discharge-stage coupling through simple linear relationships rather than complex nonlinear functions.

2. *Multiplicative-to-additive noise conversion..* Hydrological measurement errors are often proportional to magnitude (e.g., 5% uncertainty applies to both 10 ft³/s and 10,000 ft³/s). In linear space, this multiplicative noise has magnitude-dependent variance:

$$\text{Var}(Q_{\text{measured}}) = (0.05 \cdot Q_{\text{true}})^2 \quad (\text{A.3})$$

The log transformation converts multiplicative noise to additive noise with constant variance:

$$\text{Var}(\ln Q_{\text{measured}}) \approx \text{const} \quad (\text{A.4})$$

3. *Heteroscedasticity stabilization..* Without log transformation, gradient magnitudes for a 10% error on a large river exceed those for small streams by 10³-10⁶×, preventing convergence. The log transformation ensures equal-percentage errors produce equal-magnitude gradients regardless of absolute scale.

Appendix A.0.2. Tier 2: Site-Specific Standardization

For each site s , we compute normalization statistics exclusively from that site’s training partition:

$$\mu_s = \mathbb{E}_{t \in \text{train}(s)}[\mathbf{x}_t^{(1)}], \quad \sigma_s = \text{Std}_{t \in \text{train}(s)}[\mathbf{x}_t^{(1)}] \quad (\text{A.5})$$

and transform:

$$\mathbf{x}_t^{(2)} = \frac{\mathbf{x}_t^{(1)} - \mu_s}{\sigma_s + \epsilon} \quad (\text{A.6})$$

with $\epsilon = 10^{-8}$ for numerical stability.

Critical implementation detail - preventing data leakage: For sites appearing only in validation or test partitions, we substitute *global training statistics* computed over all training sites:

$$\mu_{\text{global}} = \mathbb{E}_{s \in \text{train}} \mathbb{E}_{t \in \text{train}(s)} [\mathbf{x}_t^{(1)}], \quad \sigma_{\text{global}} = \text{Std}_{s \in \text{train}} \text{Std}_{t \in \text{train}(s)} [\mathbf{x}_t^{(1)}] \quad (\text{A.7})$$

This ensures *strict partition separation*—validation and test data never influences normalization parameters. Most multi-site hydrological models violate this principle by computing statistics over all sites (including validation/test), creating subtle information leakage.

Rationale: Site-specific standardization enables weight sharing across basins by placing each site’s typical range in a common normalized space, preventing large rivers from dominating the loss landscape. A small stream with $Q \in [1, 10]$ ft³/s and the Mississippi River with $Q \in [10^4, 10^6]$ ft³/s both normalize to $\approx [-2, +2]$, contributing equally to gradient updates.

Appendix A.0.3. Tier 3: Global Clipping

To downweight extreme leverage points (measurement spikes, brief sensor failures, telemetry errors), we clip standardized variables to a symmetric bound:

$$\mathbf{x}_t^{\text{norm}} = \text{clip}(\mathbf{x}_t^{(2)}, -\tau, +\tau), \quad \tau = 3.0 \quad (\text{A.8})$$

Critical asymmetry: Clipping applies *only to inputs* during training. Predicted outputs are denormalized *without clipping* to avoid artificially truncating physical predictions.

Rationale: For normally distributed standardized variables, $\tau = 3.0$ retains approximately 99.7% of values while capping extreme outliers. In long 576-hour sequences, even rare extreme values can cause gradient explosion. Clipping provides numerical stability while preserving the network’s ability to reconstruct full-range physical magnitudes through the exact inverse mapping.

Appendix A.0.4. Exact Inverse Mapping

Let $\hat{y}^{\text{norm}} \in \mathbb{R}^{12}$ denote a model output on the normalized scale. Recovery to physical units follows the reverse transformation chain:

$$\hat{y}^{(1)} = \hat{y}^{\text{norm}} \cdot (\sigma_s + \epsilon) + \mu_s \quad (\text{A.9})$$

$$\hat{y} = \exp(\hat{y}^{(1)}) - \epsilon \quad (\text{A.10})$$

where Eq. A.9 reverses standardization and Eq. A.10 reverses log transformation.

Special cases:

- If site s used global statistics during normalization (validation/test site), apply the same global statistics in the inverse
- Static variables never log-transformed (latitude, longitude, elevation, drainage area) skip Eq. A.10

Numerical verification: We verify exact invertibility by round-trip transformation:

$$\|\mathbf{x}_{\text{original}} - \text{denorm}(\text{norm}(\mathbf{x}_{\text{original}}))\|_{\infty} < 10^{-6} \quad (\text{A.11})$$

for all training, validation, and test sequences.

Appendix A.0.5. Scale Embeddings

The scale embeddings $\{\sigma_{\ln Q,s}, \sigma_{\ln H,s}\}$ complete the normalization system by returning information about absolute variability lost during standardization:

$$\sigma_{\ln Q,s} = \text{Std}_{t \in \text{train}(s)}[\ln(Q_t + \epsilon)], \quad \sigma_{\ln H,s} = \text{Std}_{t \in \text{train}(s)}[\ln(H_t + \epsilon)] \quad (\text{A.12})$$

These embeddings are broadcast across the temporal dimension and concatenated with the normalized features \mathbf{x}^{norm} , enabling the network to condition on absolute scale.

Rationale: After site-specific standardization, a normalized discharge value of +1.0 is ambiguous—it could represent 10 ft³/s at a small headwater stream or 10,000 ft³/s at a large river. Both appear identical in normalized space. The scale embeddings resolve this ambiguity, enabling the network to express scale-dependent behavior (e.g., flashiness in small basins, baseflow dominance in large rivers) despite operating in normalized space.

Design choice validation: Ablation studies (Section 5.4) show that removing scale embeddings degrades performance by 12-15% F1 score, confirming their necessity for continental-scale learning.

Appendix B. Architecture Equations

This appendix provides complete mathematical formulations for the TCN-Transformer backbone described in Section 3.2.1.

Appendix B.1. TCN Encoder

The dilated convolution operation for sequence \mathbf{x} with filter \mathbf{f} and dilation rate r :

$$(\mathbf{x} *_r \mathbf{f})(t) = \sum_{i=0}^{k-1} f(i) \cdot x_{t-r \cdot i} \quad (\text{B.1})$$

Linear projection from input to hidden dimension:

$$\mathbf{H}^{(0)} = \mathbf{X}\mathbf{W}_{\text{proj}} + \mathbf{b}_{\text{proj}}, \quad \mathbf{W}_{\text{proj}} \in \mathbb{R}^{128 \times 128} \quad (\text{B.2})$$

TCN block with residual connection:

$$\text{TCN-Block}(\mathbf{H}, r) = \mathbf{H} + \mathcal{F}(\mathbf{H}, r) \quad (\text{B.3})$$

where $\mathcal{F}(\mathbf{H}, r) = \text{Conv1D}_r(\text{ReLU}(\text{BN}(\text{Conv1D}_r(\mathbf{H}))))$.

Receptive field at block ℓ :

$$\text{RF}_\ell = 2^{\ell+2} - 3 \quad (\text{B.4})$$

Appendix B.2. Transformer

Projection to transformer dimension:

$$\mathbf{Z}^{(0)} = \mathbf{H}^{(4)}\mathbf{W}_{\text{up}} + \mathbf{b}_{\text{up}}, \quad \mathbf{W}_{\text{up}} \in \mathbb{R}^{128 \times 256} \quad (\text{B.5})$$

Query, key, value projections for head h :

$$\mathbf{Q}_h = \mathbf{Z}\mathbf{W}_{Q,h}, \quad \mathbf{K}_h = \mathbf{Z}\mathbf{W}_{K,h}, \quad \mathbf{V}_h = \mathbf{Z}\mathbf{W}_{V,h} \quad (\text{B.6})$$

L2 normalization for cosine similarity:

$$\hat{\mathbf{q}}_i = \frac{\mathbf{q}_i}{\|\mathbf{q}_i\|_2 + \epsilon}, \quad \hat{\mathbf{k}}_j = \frac{\mathbf{k}_j}{\|\mathbf{k}_j\|_2 + \epsilon} \quad (\text{B.7})$$

Attention scores with temporal decay and causal mask:

$$\mathbf{A}_{ij} = \frac{\hat{\mathbf{q}}_i^T \hat{\mathbf{k}}_j}{\sqrt{d_h}} \cdot \gamma^{|i-j|} \cdot \mathbb{1}_{i \geq j} \quad (\text{B.8})$$

Multi-head attention:

$$\text{MultiHead}(\mathbf{Z}) = \text{Concat}(\text{head}_1, \dots, \text{head}_8)\mathbf{W}_O \quad (\text{B.9})$$

Feed-forward network:

$$\text{FFN}(\mathbf{x}) = \text{GELU}(\mathbf{x}\mathbf{W}_1 + \mathbf{b}_1)\mathbf{W}_2 + \mathbf{b}_2 \quad (\text{B.10})$$

Layer normalization:

$$\text{LayerNorm}(\mathbf{x}) = \frac{\mathbf{x} - \mu}{\sqrt{\sigma^2 + \epsilon}} \cdot \gamma + \beta \quad (\text{B.11})$$

Appendix B.3. Decoder and Skip Connections

Decoder projection:

$$\mathbf{G}^{(0)} = \mathbf{Z}^{(L)} \mathbf{W}_{\text{down}} + \mathbf{b}_{\text{down}}, \quad \mathbf{W}_{\text{down}} \in \mathbb{R}^{256 \times 128} \quad (\text{B.12})$$

Final output projection:

$$\hat{\mathbf{X}}_{\text{decoder}} = \mathbf{G}^{(4)} \mathbf{W}_{\text{out}} + \mathbf{b}_{\text{out}}, \quad \mathbf{W}_{\text{out}} \in \mathbb{R}^{128 \times 12} \quad (\text{B.13})$$

Gated skip connection:

$$\hat{\mathbf{X}} = (1 - \sigma(\alpha)) \cdot \hat{\mathbf{X}}_{\text{decoder}} + \sigma(\alpha) \cdot \text{Linear}(\mathbf{H}_{\text{encoder}}^{(4)}) \quad (\text{B.14})$$

Appendix C. Loss Functions

Appendix C.1. Pretraining Loss

Combined pretraining objective:

$$\mathcal{L}_{\text{pretrain}} = \mathcal{L}_{\text{recon}} + 0.6\mathcal{L}_{\text{temporal}} + 0.4\mathcal{L}_{\text{variance}} + 0.3\mathcal{L}_{\text{scale}} + 0.05\mathcal{L}_{\text{diversity}} \quad (\text{C.1})$$

Weighted reconstruction loss:

$$\mathcal{L}_{\text{recon}} = \frac{1}{T} \sum_{t=1}^T \sum_{f=1}^d w_f \cdot (\hat{x}_{t,f} - x_{t,f})^2 \quad (\text{C.2})$$

with weights $w = 3.0$ (discharge), 2.5 (stage), 1.5 (seasonal), 1.0 (static).

Temporal consistency loss:

$$\mathcal{L}_{\text{temporal}} = \frac{1}{T-1} \sum_{t=1}^{T-1} \sum_{f \in \{Q,H\}} w_f \cdot [(\hat{x}_{t+1,f} - \hat{x}_{t,f}) - (x_{t+1,f} - x_{t,f})]^2 \quad (\text{C.3})$$

Variance preservation loss:

$$\mathcal{L}_{\text{variance}} = \sum_{f=1}^d [\text{Var}(\hat{\mathbf{x}}_f) - \text{Var}(\mathbf{x}_f)]^2 \quad (\text{C.4})$$

Scale consistency loss:

$$\mathcal{L}_{\text{scale}} = \frac{1}{T} \sum_{t=1}^T \sum_{f \in \text{scale}} (\hat{x}_{t,f} - x_{t,f})^2 \quad (\text{C.5})$$

Diversity regularization:

$$\mathcal{L}_{\text{diversity}} = -\text{Entropy}(\mathbf{A}) + \lambda_{\text{rank}} \max(0, 10 - \text{rank}(\mathbf{H})) \quad (\text{C.6})$$

Appendix C.2. Fine-Tuning Loss

Focal loss for detection:

$$\mathcal{L}_{\text{focal}} = -\frac{1}{T} \sum_{t=1}^T \alpha_t (1 - \hat{p}_t)^\gamma [y_t \log \hat{p}_t + (1 - y_t) \log(1 - \hat{p}_t)] \quad (\text{C.7})$$

with $\alpha = 0.25$, $\gamma = 2.0$.

Corruption reconstruction loss:

$$\mathcal{L}_{\text{corrupt}} = \frac{1}{|\mathcal{T}_{\text{anom}}|} \sum_{t \in \mathcal{T}_{\text{anom}}} \|\hat{\mathbf{X}}_t - \mathbf{X}_t^{(\text{clean})}\|_2^2 \quad (\text{C.8})$$

Clean preservation loss:

$$\mathcal{L}_{\text{preserve}} = \frac{1}{|\mathcal{T}_{\text{clean}}|} \sum_{t \in \mathcal{T}_{\text{clean}}} \|\hat{\mathbf{X}}_t - \mathbf{X}_t^{(\text{obs})}\|_2^2 \quad (\text{C.9})$$

Physics constraint loss:

$$\mathcal{L}_{\text{physics}} = \frac{1}{T-1} \sum_{t=1}^{T-1} \text{ReLU}(-\nabla_t Q \cdot \nabla_t H) + \lambda_{\text{RC}} \mathbb{E}[d_{\text{RC}}] \quad (\text{C.10})$$

Combined fine-tuning objective:

$$\mathcal{L}_{\text{finetune}} = 1.5\mathcal{L}_{\text{focal}} + \lambda_c(\epsilon)\mathcal{L}_{\text{corrupt}} + \lambda_p(\epsilon)\mathcal{L}_{\text{preserve}} + 0.1\mathcal{L}_{\text{physics}} \quad (\text{C.11})$$

with $\lambda_c(\epsilon) = 0.25 \cdot \min(1, \epsilon/3)$ and $\lambda_p(\epsilon) = 0.05 \cdot \min(1, \epsilon/3)$.

Appendix D. Quality Control Protocols

This appendix details the multi-tier quality control protocol applied to ensure training data integrity (Section 2.1.3).

Appendix D.0.1. Outlier Detection

Values exceeding four standard deviations from site-specific monthly means are flagged for manual review:

$$\text{flag}(Q_t) = \mathbb{I}[|Q_t - \mu_{Q,m(t),s}| > 4\sigma_{Q,m(t),s}] \quad (\text{D.1})$$

where $m(t)$ denotes the month of timestep t , and $\mu_{Q,m,s}$, $\sigma_{Q,m,s}$ are computed from all observations in month m for site s within the training period.

Rationale: The adaptive monthly threshold accounts for natural hydrologic variability (e.g., higher variance during spring snowmelt) while identifying extreme leverage points. Fixed global thresholds would flag normal high flows in flashy basins while missing subtle anomalies in stable systems.

Appendix D.0.2. Physical Plausibility Checks

Temporal consistency. We test rate-of-change using a site-specific threshold:

$$\frac{|Q_t - Q_{t-1}|}{Q_{t-1}} > \theta_{\text{site}} \quad (\text{D.2})$$

where θ_{site} is computed as the 99th percentile of observed fractional changes during the training period for that site. This adaptive threshold accommodates both flashy small basins and slowly-responding large systems.

Rating curve validation. Stage-discharge pairs are validated against the power-law rating form $Q = a(H - H_0)^b$ [39]. We fit this relationship using robust regression (RANSAC with 1000 iterations, inlier threshold 15%) on each site’s training data, then flag pairs deviating beyond $2\times$ the fitted residual standard deviation.

Range bounds. All values are checked against physically plausible ranges:

- Discharge: $Q \in [0, Q_{\max}]$ where $Q_{\max} = \max(\text{training data}) \times 2.0$
- Stage: $H \in [H_{\min} - 1.0, H_{\max} + 1.0]$ ft, allowing 1-foot exceedance beyond observed training range

Appendix D.0.3. Gap Filling Strategy

Short gaps (1-6 hours): Linear interpolation.

$$Q_t = Q_{t_0} + (Q_{t_1} - Q_{t_0}) \cdot \frac{t - t_0}{t_1 - t_0} \quad (\text{D.3})$$

where t_0 and t_1 are the last valid timestep before and first valid timestep after the gap.

Rationale: Linear interpolation is appropriate for slowly-varying base-flow conditions where discharge changes smoothly. For 1-6 hour gaps, this assumption typically holds.

Medium gaps (6-24 hours): Exponential recession model. For gaps exceeding 6 hours but less than 24 hours, we apply the exponential recession relationship [41, 42]:

$$Q(t) = Q(t_0) \exp[-k(t - t_0)] \quad (\text{D.4})$$

The recession constant k is estimated via:

$$k = -\frac{1}{\Delta t} \ln \left(\frac{Q(t_0 + \Delta t)}{Q(t_0)} \right) \quad (\text{D.5})$$

using a 48-hour window before the gap. If insufficient pre-gap data exists, we use the site-specific median recession constant computed from all valid recession segments in the training period.

Rationale: The exponential form respects fundamental watershed storage dynamics: $\frac{dS}{dt} = -kS$, where storage S is linearly related to discharge. This is more physically realistic than linear interpolation for medium-duration gaps where recession behavior dominates.

Long gaps (>24 hours): Exclusion. Gaps exceeding 24 hours are excluded entirely from sequence construction. No imputation is attempted to prevent long-range artifacts that could introduce spurious patterns.

Appendix D.0.4. Gap Statistics

The complete gap-filling protocol retains 94.7% of potential 576-hour sequences:

- 89.3% contain *no* interpolation
- 9.8% contain 1-3 interpolated hours (linear)
- 0.9% contain 4-6 hours (mix of linear and recession)
- 0% contain >6 hours (sequences intersecting gaps >6h are dropped)

Leakage prevention: Any sequence window intersecting a flagged timestep (outlier, physical implausibility, or gap >6h) is excluded entirely, even if only a single hour is affected. This conservative approach eliminates potential information leakage from imputation.

Appendix E. Training-Time Anomaly Injection

This appendix provides implementation details for the on-the-fly synthetic anomaly injection during training (Section 2.3).

Appendix E.0.1. Simplified Anomaly Types

The training injector implements approximately 11 simplified corruption patterns applied in normalized log-space:

1. **Spike:** Add Gaussian noise impulses: $x'_t = x_t + \mathcal{N}(0, \alpha\sigma_x)$ at random positions, $\alpha \sim U(2, 5)$
2. **Drift:** Apply linear trend: $x'_t = x_t + \beta \cdot (t - t_{\text{start}})$ where $\beta \sim U(-0.01, +0.01)$
3. **Flatline:** Freeze values: $x'_t = x_{t_{\text{freeze}}}$ for all t in segment
4. **Dropout:** Replace with near-zero: $x'_t = \epsilon$ where $\epsilon \sim U(10^{-6}, 10^{-4})$
5. **Saturation:** Clip to limits: $x'_t = \text{clip}(x_t, x_{\text{min}} + 0.1, x_{\text{max}} - 0.1)$
6. **Clock shift:** Temporal offset: $x'_t = x_{t+\Delta t}$ where $\Delta t \sim \{-3, -2, -1, +1, +2, +3\}$ hours
7. **Quantization:** Discretize: $x'_t = \text{round}(x_t/\Delta q) \cdot \Delta q$ where $\Delta q \sim U(0.05, 0.2)$
8. **Unit jump:** Abrupt bias: $x'_t = x_t + \gamma$ where $\gamma \sim U(-1.0, +1.0)$
9. **Temporal warp:** Stretch/compress: resample segment via $t' = t_{\text{start}} + (t - t_{\text{start}}) \cdot w$ where $w \sim U(0.8, 1.2)$
10. **Splice:** Replace segment with values from different time: $\mathbf{x}'_{t_1:t_2} = \mathbf{x}_{t_3:t_3+(t_2-t_1)}$
11. **Subtle drift:** Very gentle linear trend: $x'_t = x_t + \beta \cdot (t - t_{\text{start}})$ where $\beta \sim U(-0.002, +0.002)$

These simple transformations contrast sharply with test-time physical-space injections using multi-variant equations (exponential/sigmoid/polynomial drift, hydraulic-coupled ice effects, etc.).

Appendix E.0.2. Coverage Control Algorithm

To achieve target coverage c_{target} (e.g., 10% for light tier, 20% for moderate tier), the injector uses iterative refinement:

1. Initialize: $n_{\text{segments}} \sim U(2, 4)$, strength $\alpha = 1.0$

2. For attempt = 1 to 3:
 - (a) Generate n_{segments} anomaly segments with strength α
 - (b) Compute realized coverage c_{realized}
 - (c) If $|c_{\text{realized}} - c_{\text{target}}| < \delta$: return corrupted sequence
 - (d) Else if $c_{\text{realized}} < c_{\text{target}}$: $\alpha \leftarrow \alpha \times U(1.1, 1.4)$
 - (e) Else: $\alpha \leftarrow \alpha \times U(0.7, 0.9)$
3. Return best attempt (closest to target)

This adaptive mechanism maintains mean realized coverage $15.2\% \pm 3.1\%$ across batches regardless of sequence characteristics.

Appendix F. Test-Time Anomaly Injection

This appendix provides complete mathematical formulations for the 18 test anomaly types, each with 3-4 equation variants.

Appendix F.0.1. Example: Drift Anomaly (4 variants)

Variant 1 - Linear:

$$Q'(t) = Q(t) + \beta_Q \cdot (t - t_{\text{start}}), \quad H'(t) = H(t) + \beta_H \cdot (t - t_{\text{start}}) \quad (\text{F.1})$$

where $\beta_Q \sim U(-0.5, +0.5) \text{ ft}^3/\text{s}/\text{hr}$, $\beta_H \sim U(-0.01, +0.01) \text{ ft}/\text{hr}$

Variant 2 - Exponential:

$$Q'(t) = Q(t) \cdot \exp[\alpha_Q \cdot (t - t_{\text{start}})], \quad H'(t) = H(t) \cdot \exp[\alpha_H \cdot (t - t_{\text{start}})] \quad (\text{F.2})$$

where $\alpha_Q \sim U(-0.01, +0.01) \text{ hr}^{-1}$, $\alpha_H \sim U(-0.005, +0.005) \text{ hr}^{-1}$

Variant 3 - Sigmoid:

$$Q'(t) = Q(t) + \Delta Q \cdot \frac{1}{1 + \exp[-k_Q(t - t_{\text{mid}})]}, \quad H'(t) = H(t) + \Delta H \cdot \frac{1}{1 + \exp[-k_H(t - t_{\text{mid}})]} \quad (\text{F.3})$$

where $t_{\text{mid}} = (t_{\text{start}} + t_{\text{end}})/2$, $\Delta Q \sim U(-Q_{\text{mean}}/2, +Q_{\text{mean}}/2)$, $k_Q \sim U(0.1, 0.5)$

Variant 4 - Polynomial:

$$Q'(t) = Q(t) + [a_Q(t - t_{\text{start}})^2 + b_Q(t - t_{\text{start}})], \quad \text{similarly for } H \quad (\text{F.4})$$

where coefficients a, b chosen to achieve target endpoint deviation $\sim U(0.1Q_{\text{mean}}, 0.3Q_{\text{mean}})$

Appendix F.0.2. Example: Ice Backwater (3 variants)

Variant 1 - Gradual onset:

$$\alpha_{\text{ice}}(t) = \alpha_{\text{max}} \cdot \frac{t - t_{\text{start}}}{t_{\text{peak}} - t_{\text{start}}} \quad \text{for } t \in [t_{\text{start}}, t_{\text{peak}}] \quad (\text{F.5})$$

$$H'(t) = H(t) \cdot [1 + \alpha_{\text{ice}}(t)] \quad (\text{F.6})$$

$$Q'(t) = Q(t) \cdot [1 - \beta_{\text{ice}}(t)] \quad (\text{F.7})$$

where $\alpha_{\text{max}} \sim U(0.15, 0.55)$, $\beta_{\text{max}} \sim U(0, 0.10)$, $t_{\text{peak}} - t_{\text{start}} \sim U(12, 48)$ hours

Variant 2 - Abrupt onset, gradual recovery:

$$\alpha_{\text{ice}}(t) = \begin{cases} \alpha_{\text{max}} & t \in [t_{\text{start}}, t_{\text{recover}}] \\ \alpha_{\text{max}} \cdot \exp[-k(t - t_{\text{recover}})] & t > t_{\text{recover}} \end{cases} \quad (\text{F.8})$$

where $k \sim U(0.01, 0.05) \text{ hr}^{-1}$

Variant 3 - Periodic breakup events:

$$\alpha_{\text{ice}}(t) = \alpha_{\text{base}} + \sum_{i=1}^{N_{\text{events}}} A_i \exp\left[-\frac{(t - t_i)^2}{2\sigma_i^2}\right] \quad (\text{F.9})$$

where $\alpha_{\text{base}} \sim U(0.2, 0.4)$, $N_{\text{events}} \sim U(2, 5)$, event amplitudes $A_i \sim U(-0.3, -0.1)$ (negative for breakup), widths $\sigma_i \sim U(1, 6)$ hours

Appendix G. Expert Review Documentation

This appendix documents the structured expert review process for synthetic anomaly validation.

Appendix G.0.1. Review Protocol

Domain experts evaluated each anomaly type using standardized forms. Reviewers included:

- A faculty member in geoscience with extensive experience in water resources and hydrological research
- A research assistant from the University of Vermont Water Resources Institute with operational experience from a USGS internship, including exposure to real-world streamflow data quality challenges

Realism assessment (4-point scale):

- 4 - Very realistic: Commonly observed in operational QA/QC work-flows
- 3 - Realistic: Plausible, occasionally observed
- 2 - Questionable: Theoretically possible but rarely encountered
- 1 - Unrealistic: Does not match field experience

Temporal scale validation: For each anomaly type, reviewers identified duration ranges appearing implausible relative to operational experience. For example, ice backwater durations <24 hours were flagged as too brief for realistic ice formation/breakup dynamics.

Confound detection: Reviewers flagged injection regimes creating:

- Artificially easy detection (e.g., spike magnitudes $> 10\sigma$ never observed in practice)
- Ambiguous labeling (e.g., patterns indistinguishable from natural variability)
- Physical impossibilities (e.g., rating curve violations)

Appendix G.0.2. Key Feedback Integration

Table G.9 documents major revisions based on expert feedback.

Appendix G.0.3. Consensus Categorization

The final 18-type taxonomy reflects reviewer agreement on field-relevance:

High confidence (9 types): All reviewers rated 3-4 (realistic to very realistic), with specific operational examples provided:

- Dropout: Battery failure, telemetry loss
- Flatline: Frozen float, clogged intake
- Ice backwater: Common Nov-Apr northern stations
- Rating drift: Frequent after major floods, channel migration

Table G.9: Expert feedback integration

Topic	Initial	Expert Feedback	Change Made
Ice duration	Macro: 72-144h	Ice persists weeks-months in northern systems	Extended to 72-520h
Backwater onset	50% instantaneous	Backwater develops gradually as obstruction forms	All use gradual onset (>6h)
Spike magnitudes	Some $> 8\sigma$	Never see such extremes in approved data	Capped at 5σ
Coverage tier	40% probability	Reduce for challenging evaluation	Reduced to 20%
Equation variants	Some had 2	Need stronger separation for generalization claims	Minimum 3 per type
Drift subtlety	All $> 0.1 \text{ ft}^3\text{s}^{-1}\text{day}^{-1}$	Drift can be much more subtle	Added subtle variant

Medium confidence (4 types): Mixed ratings (2-4), considered plausible but less frequently documented:

- Time misalignment: Possible with manual data entry, rare in modern systems
- Gate operation: Relevant for regulated sites, not universal

Low confidence (4 types): Majority rated 2 (questionable), retained for completeness:

- Splice: Hard to imagine operational scenario
- Warp: Never seen systematic time stretching

Debated (retained with caveat): Reviewers disagreed on anomaly vs. natural variability:

- Noise burst: Could be natural turbulence or sensor issue, ambiguous

Appendix H. Canadian Data Quality Filtering

This appendix details quality filtering applied to Canadian ECCC stations (Section 2.4.2).

Appendix H.0.1. Hydrologically-Motivated Checks

All checks apply to corrected series only, ensuring evaluation on windows where hydrologist-edited records behave as plausible physical time series.

1. Sufficient variability.

$$CV(H_{\text{corr}}) = \frac{\sigma(H_{\text{corr}})}{\mu(H_{\text{corr}})} > 0.10 \quad (\text{H.1})$$

Rationale: Removes nearly flat records where water level hardly changes (e.g., failed sensors reporting constant values, tidal gauges at slack water). Anomaly detection is ill-posed on essentially constant series.

2. Monotonic rating relation.

$$\rho_{\text{Spearman}}(H_{\text{corr}}, Q_{\text{corr}}) > 0.5 \quad (\text{H.2})$$

Rationale: Enforces physically plausible behavior where larger stages generally correspond to larger discharges. Violations suggest either: (a) severe data quality issues making the window unsuitable for evaluation, or (b) complex hydraulics (backwater, tidal influence) where the station may not be appropriate for standard QA/QC methods.

3. Reasonable rating curve exponent. Fit $\log Q = \log a + b \log H$ using robust regression (RANSAC), require:

$$b \in [0.5, 10] \quad (\text{H.3})$$

Rationale: Natural open-channel flow typically exhibits $b \in [1.5, 3.0]$ based on hydraulic geometry [39]. We relax to $[0.5, 10]$ to accommodate weirs ($b \approx 1.5$), rectangular channels ($b \approx 1.0$), and complex cross-sections, while excluding physically implausible extremes.

4. Moderate rating curve fit.

$$R^2 \geq 0.3 \quad (\text{H.4})$$

Rationale: Deliberately modest threshold allows hydraulic complexity (hysteresis, backwater) while removing windows where stage explains essentially none of discharge variability.

5. *Sufficient valid data fraction.*

$$\frac{\#\{t : Q_{\text{corr},t} > 0 \text{ and } H_{\text{corr},t} > 0\}}{\#\{\text{all timesteps}\}} \geq 0.70 \quad (\text{H.5})$$

Rationale: Ensures enough usable information for robust anomaly detection features. Windows with $> 30\%$ missing/invalid data lack statistical power.

6. *Limited flatline segments.* Compute consecutive differences: $\Delta H_t = |H_{\text{corr},t} - H_{\text{corr},t-1}|$. Require:

$$\frac{\#\{t : \Delta H_t < 0.001 \text{ ft}\}}{\#\{\text{all timesteps}\}} < 0.30 \quad (\text{H.6})$$

Rationale: Natural hydrographs exhibit continuous variation. If $> 30\%$ of consecutive values are identical (within 0.001 ft precision), the gauge is likely frozen or malfunctioning. This preserves low-variability baseflow periods while removing structural sensor failures.

Appendix H.0.2. Station-Level Filtering

After temporal alignment of the four series (stage raw/corrected, discharge raw/corrected), we compute missing data fraction:

$$f_{\text{missing}} = \frac{\#\{\text{timesteps missing any of 4 series}\}}{\#\{\text{all timesteps}\}} \quad (\text{H.7})$$

Stations with $f_{\text{missing}} > 0.05$ (losing $> 5\%$ of hourly timesteps) are excluded entirely from the Canadian test set.

Rationale: High missing data rates indicate either: (a) inconsistent data collection between raw and corrected archives, or (b) stations undergoing major operational changes. Both scenarios compromise evaluation validity.

Appendix H.0.3. Filtering Statistics

Across the full ECCC archive:

- Initial stations with raw + corrected data: 1,847
- After station-level filtering ($< 5\%$ missing): 1,203 (65.1% retention)
- After window-level filtering (6 criteria): 487 stations with eligible windows (26.4% overall retention)

- Random sampling for evaluation: 100 stations

The conservative filtering ensures evaluation on high-quality, hydrologically meaningful windows where model performance reflects genuine anomaly detection capability rather than artifacts of poor data quality.

References

- [1] F. Kratzert, D. Klotz, M. Herrnegger, A. K. Sampson, S. Hochreiter, G. S. Nearing, Toward improved predictions in ungauged basins: Exploiting the power of machine learning, *Water Resources Research* 55 (12) (2019) 11344–11354. doi:10.1029/2019WR026065.
- [2] F. Kratzert, G. Nearing, N. Addor, T. Erickson, M. Gauch, O. Gilon, L. Gudmundsson, A. Hassidim, D. Klotz, S. Nevo, G. Shalev, Y. Matias, Caravan - a global community dataset for large-sample hydrology, *Scientific Data* 10 (1) (2023) 61. doi:10.1038/s41597-023-01975-w.
- [3] G. Sterle, J. Perdril, D. W. Kincaid, K. L. Underwood, D. M. Rizzo, I. U. Haq, L. Li, B. S. Lee, T. Adler, H. Wen, H. Middleton, A. A. Harpold, CAMELS-Chem: augmenting CAMELS (Catchment Attributes and Meteorology for Large-sample Studies) with atmospheric and stream water chemistry data, *Hydrology and Earth System Sciences* 28 (3) (2024) 611–630. doi:10.5194/hess-28-611-2024.
- [4] F. Kratzert, D. Klotz, G. Shalev, G. Klambauer, S. Hochreiter, G. Nearing, Towards learning universal, regional, and local hydrological behaviors via machine learning applied to large-sample datasets, *Hydrology and Earth System Sciences* 23 (12) (2019) 5089–5110. doi:10.5194/hess-23-5089-2019.
- [5] G. S. Nearing, D. Klotz, J. M. Frame, M. Gauch, O. Gilon, F. Kratzert, A. K. Sampson, G. Shalev, S. Nevo, Technical note: Data assimilation and autoregression for using near-real-time streamflow observations in long short-term memory networks, *Hydrology and Earth System Sciences* 26 (21) (2022) 5493–5513. doi:10.5194/hess-26-5493-2022. URL <https://hess.copernicus.org/articles/26/5493/2022/>
- [6] W. Sun, B. Trevor, Ice jam formation, breakup and prediction methods based on hydroclimatic data using artificial intelligence: A review, *Cold*

Regions Science and Technology 168 (2019) 102894. doi:10.1016/j.coldregions.2019.102894.

- [7] E. M. Dogo, N. I. Nwulu, B. Twala, C. O. Aigbavboa, A survey of machine learning methods applied to anomaly detection on drinking-water quality data, *Urban Water Journal* 16 (3) (2019) 235–248. doi:10.1080/1573062X.2019.1637002.
- [8] Aquatic Informatics Inc., AQUARIUS Time-Series: Water data management software, <https://aquaticinformatics.com/products/aquarius-environmental-water-data-management/>, version X.X. Vancouver, BC, Canada (2024).
- [9] L. Schmidt, D. Schäfer, J. Geller, P. Lünenschloss, B. Palm, K. Rinke, C. Rebmann, M. Rode, J. Bumberger, System for automated quality control (SaQC) to enable traceable and reproducible data streams in environmental science, *Environmental Modelling & Software* 169 (2023) 105809. doi:10.1016/j.envsoft.2023.105809.
- [10] A. S. Jones, T. L. Jones, J. S. Horsburgh, Toward automating post processing of aquatic sensor data, *Environmental Modelling & Software* 151 (2022) 105364. doi:10.1016/j.envsoft.2022.105364.
- [11] H. K. McMillan, I. K. Westerberg, T. Krueger, Hydrological data uncertainty and its implications, *WIREs Water* 5 (6) (2018) e1319. doi:10.1002/wat2.1319.
- [12] R. Taormina, K.-w. Chau, Neural network river forecasting with multi-objective fully informed particle swarm optimization, *Journal of Hydroinformatics* 17 (1) (2015) 99–113. doi:10.2166/hydro.2014.116.
- [13] N. Addor, A. J. Newman, N. Mizukami, M. P. Clark, The CAMELS data set: catchment attributes and meteorology for large-sample studies, *Hydrology and Earth System Sciences* 21 (10) (2017) 5293–5313. doi:10.5194/hess-21-5293-2017.
- [14] A. Goldstein, A. Kapelner, J. Bleich, E. Pitkin, Peeking inside the black box: Visualizing statistical learning with plots of individual conditional expectation, *Journal of Computational and Graphical Statistics* 24 (1) (2015) 44–65. doi:10.1080/10618600.2014.907095.

- [15] M. A. Belay, S. S. Blakseth, A. Rasheed, P. Salvo Rossi, Unsupervised anomaly detection for iot-based multivariate time series: Existing solutions, performance analysis and future directions, *Sensors* 23 (5) (2023) 2844. doi:10.3390/s23052844.
- [16] H. Shi, J. Guo, Y. Deng, Z. Qin, Machine learning-based anomaly detection of groundwater microdynamics: case study of chengdu, china, *Scientific Reports* 13 (2023) 14718. doi:10.1038/s41598-023-38447-5.
- [17] V. Nourani, A. H. Baghanam, J. Adamowski, O. Kisi, Applications of hybrid wavelet–artificial intelligence models in hydrology: A review, *Journal of Hydrology* 514 (2014) 358–377. doi:10.1016/j.jhydro.2014.03.057.
- [18] S. Hochreiter, J. Schmidhuber, Long short-term memory, *Neural Computation* 9 (8) (1997) 1735–1780. doi:10.1162/neco.1997.9.8.1735.
- [19] Y. He, J. Zhao, Temporal convolutional networks for anomaly detection in time series, in: *Journal of Physics: Conference Series*, Vol. 1213, IOP Publishing, 2019, p. 042050. doi:10.1088/1742-6596/1213/4/042050.
- [20] S. Han, H. Dong, A temporal window attention-based window-dependent long short-term memory network for multivariate time series prediction, *Entropy* 25 (1) (2023) 10. doi:10.3390/e25010010.
- [21] E. Osman, Detecting environmental anomalies: Variational autoencoder-based analysis of air quality time series data, *International Journal of Intelligent Systems and Applications in Engineering* 12 (4) (2024) 3687–3698.
URL <https://ijisae.org/index.php/IJISAE/article/view/6912>
- [22] Y. Lee, C. Park, N. Kim, J. Ahn, J. Jeong, LSTM-autoencoder based anomaly detection using vibration data of wind turbines, *Sensors* 24 (9) (2024) 2833. doi:10.3390/s24092833.
- [23] L. Chen, H. Jiang, L. Wang, J. Li, M. Yu, Y. Shen, X. Du, Generative adversarial synthetic neighbors-based unsupervised anomaly detection, *Scientific Reports* 15 (1) (2025) 16. doi:10.1038/s41598-024-84863-6.

- [24] H. Kim, C. Lee, Enhancing anomaly detection via generating diversified and hard-to-distinguish synthetic anomalies, in: Proceedings of the 33rd ACM International Conference on Information and Knowledge Management, CIKM '24, ACM, Boise, ID, USA, 2024, pp. 2542–2551. doi:10.1145/3627673.3679623.
- [25] T. Lees, M. Buechel, B. Anderson, L. Slater, S. Reece, G. Coxon, S. J. Dadson, Benchmarking data-driven rainfall–runoff models in great britain: a comparison of long short-term memory (lstm)-based models with four lumped conceptual models, *Hydrology and Earth System Sciences* 25 (10) (2021) 5517–5534. doi:10.5194/hess-25-5517-2021. URL <https://hess.copernicus.org/articles/25/5517/2021/>
- [26] J. Devlin, M.-W. Chang, K. Lee, K. Toutanova, BERT: Pre-training of deep bidirectional transformers for language understanding, in: Proceedings of the 2019 Conference of the North American Chapter of the Association for Computational Linguistics: Human Language Technologies (NAACL-HLT), Association for Computational Linguistics, 2019, pp. 4171–4186. doi:10.18653/v1/N19-1423.
- [27] S. Dooley, G. S. Khurana, C. Mohapatra, S. V. Naidu, C. White, Forecastpfn: Synthetically-trained zero-shot forecasting, in: Advances in Neural Information Processing Systems, Vol. 36, 2023, pp. 24937–24955.
- [28] T. Nguyen, J. Brandstetter, A. Kapoor, J. K. Gupta, A. Grover, Climax: A foundation model for weather and climate, in: Proceedings of the 40th International Conference on Machine Learning, Vol. 202 of Proceedings of Machine Learning Research, PMLR, 2023, pp. 18605–18646. URL <https://proceedings.mlr.press/v202/nguyen23a.html>
- [29] J. Pathak, S. Subramanian, P. Harrington, S. Raja, A. Chattopadhyay, M. Mardani, T. Kurth, D. Hall, Z. Li, K. Azizzadenesheli, et al., Fourcastnet: A global data-driven high-resolution weather model using adaptive fourier neural operators, arXiv preprint arXiv:2202.11214 (2022).
- [30] R. Lam, A. Sanchez-Gonzalez, M. Willson, P. Wirnsberger, M. Fortunato, F. Alet, S. Ravuri, T. Ewalds, Z. Eaton-Rosen, W. Hu, A. Merose, S. Hoyer, G. Holland, O. Vinyals, J. Stott, A. Pritzel, S. Mohamed, P. Battaglia, Learning skillful medium-range global weather forecasting, *Science* 382 (6677) (2023) 1416–1421. doi:10.1126/science.adi2336.

- [31] K. Bi, L. Xie, H. Zhang, X. Chen, X. Gu, Q. Tian, Accurate medium-range global weather forecasting with 3d neural networks, *Nature* 619 (7970) (2023) 533–538. doi:10.1038/s41586-023-06185-3.
- [32] J. Schmude, S. Roy, W. Trojak, J. Jakubik, D. S. Civitarese, S. Singh, J. Kuehnert, K. Ankur, A. Gupta, C. E. Phillips, R. Kienzler, D. Szwarcman, V. Gaur, R. Shinde, R. Lal, A. D. Silva, J. L. G. Diaz, A. Jones, S. Pfreundschuh, A. Lin, A. Sheshadri, U. Nair, V. Anantharaj, H. Hamann, C. Watson, M. Maskey, T. J. Lee, J. B. Moreno, R. Ramachandran, Prithvi wxc: Foundation model for weather and climate (2024). arXiv:2409.13598.
- [33] X. Wang, S. Liu, A. Tsaris, J. Y. Choi, A. M. Aji, M. Fan, W. Zhang, M. Ashfaq, D. Lu, P. Balaprakash, J. Yin, ORBIT: Oak Ridge Base foundation model for earth system predictability, in: *Proceedings of the International Conference for High Performance Computing, Networking, Storage and Analysis (SC24)*, IEEE, 2024. doi:10.1109/SC41406.2024.00007.
- [34] M. Gauch, J. Mai, J. Lin, The proper care and feeding of camels: How limited training data affects streamflow prediction, *Environmental Modelling & Software* 135 (2021) 104926. doi:10.1016/j.envsoft.2020.104926.
- [35] M. A. Ali, L. B. Roy, M. I. Balya, N. Deka, K. Tamilvanan, M. Renukhadevi, Environmental monitoring using satellite imagery and deep learning technique, *International Journal of Environmental Sciences* 11 (24s) (2025) 4808–4816.
URL <https://theaspd.com/index.php/ijes/article/download/11055/7939/23276>
- [36] I. Goodfellow, Y. Bengio, A. Courville, *Deep learning*, MIT Press, 2016.
- [37] I. Deznabi, P. Kumar, M. Fiterau, Zero-shot microclimate prediction with deep learning, arXiv preprint arXiv:2401.02665 (2024).
- [38] U.S. Geological Survey, USGS water data for the nation, National Water Information System, accessed: 2024-XX-XX (2024).
URL <https://waterdata.usgs.gov/nwis>

- [39] V. T. Chow, D. R. Maidment, L. W. Mays, *Applied Hydrology*, 1st Edition, McGraw-Hill, New York, 1988.
- [40] R. W. Herschy (Ed.), *Hydrometry: Principles and Practices*, 2nd Edition, John Wiley & Sons, Chichester, 1999.
- [41] R. M. Vogel, C. N. Kroll, Regional geohydrologic-geomorphic relationships for the estimation of low-flow statistics, *Water Resources Research* 28 (9) (1992) 2451–2458. doi:10.1029/92WR01007.
- [42] L. M. Tallaksen, A review of baseflow recession analysis, *Journal of Hydrology* 165 (1-4) (1995) 349–370. doi:10.1016/0022-1694(94)02540-R.
- [43] A. Vaswani, N. Shazeer, N. Parmar, J. Uszkoreit, L. Jones, A. N. Gomez, Ł. Kaiser, I. Polosukhin, Attention is all you need, in: *Advances in Neural Information Processing Systems*, Vol. 30, 2017, pp. 5998–6008.
- [44] J. A. Nittrouer, Backwater hydrodynamics and sediment transport in the lowermost Mississippi River Delta: Implications for the development of fluvial-deltaic landforms in a large lowland river, in: *Deltas: Landforms, Ecosystems and Human Activities*, Proceedings of the HP1, IAHS-IAPSO-IASPEI Assembly, Vol. 358 of IAHS Publication, IAHS Press, Gothenburg, Sweden, 2013, pp. 48–61.
- [45] B. P. Sangal, A. K. Biswas, The 3-parameter lognormal distribution and its applications in hydrology, *Water Resources Research* 6 (2) (1970) 505–515. doi:10.1029/WR006i002p00505.
- [46] H. S. Santeford, G. R. Alger, J. A. Stark, Ice in streams: Its formation and effects on flow, *Water-Resources Investigations Report 86-4209*, U.S. Geological Survey, Lansing, Michigan (1986).
URL <https://pubs.usgs.gov/wri/1986/4209/report.pdf>
- [47] K. He, X. Chen, S. Xie, Y. Li, P. Dollár, R. Girshick, Masked autoencoders are scalable vision learners, in: *Proceedings of the IEEE/CVF Conference on Computer Vision and Pattern Recognition (CVPR)*, 2022, pp. 16000–16009. doi:10.1109/CVPR52688.2022.01553.

- [48] F. Zhuang, Z. Qi, K. Duan, D. Xi, Y. Zhu, H. Zhu, H. Xiong, Q. He, A comprehensive survey on transfer learning, *Proceedings of the IEEE* 109 (1) (2021) 43–76. doi:10.1109/JPROC.2020.3004555.
- [49] G. Mongaras, T. Dohm, E. C. Larson, Cottention: Linear transformers with cosine attention, *arXiv preprint arXiv:2409.18747* (2024).
- [50] A. Wettig, T. Gao, Z. Zhong, D. Chen, Should you mask 15% in masked language modeling?, in: *Proceedings of the 17th Conference of the European Chapter of the Association for Computational Linguistics, Association for Computational Linguistics, Dubrovnik, Croatia, 2023*, pp. 2985–3000. doi:10.18653/v1/2023.eacl-main.217.
- [51] E. J. Kennedy, *Discharge Ratings at Gaging Stations, Techniques of Water-Resources Investigations, Book 3, Chapter A10*, U.S. Geological Survey, 1984.
URL <https://pubs.usgs.gov/twri/twri3-a10/>
- [52] I. Loshchilov, F. Hutter, Decoupled weight decay regularization, *arXiv preprint arXiv:1711.05101* (2017).
- [53] F. Angiulli, F. Fassetti, L. Ferragina, Reconstruction error-based anomaly detection with few outlying examples, *arXiv preprint arXiv:2305.10464* (2023).
- [54] D. Gong, L. Liu, V. Le, B. Saha, M. R. Mansour, S. Venkatesh, A. van den Hengel, Memorizing normality to detect anomaly: Memory-augmented deep autoencoder for unsupervised anomaly detection, in: *IEEE/CVF International Conference on Computer Vision (ICCV)*, 2019, pp. 1705–1714. doi:10.1109/ICCV.2019.00179.
- [55] C. E. Novak, *WRD data reports preparation guide*, Open-File Report 85-480, U.S. Geological Survey, Reston, Virginia (1985). doi:10.3133/ofr85480.
URL <https://pubs.usgs.gov/publication/ofr85480>
- [56] F. Rainville, D. Hutchinson, A. Stead, D. Moncur, D. Elliott, *Hydrometric manual – data computations: Stage-discharge model development and maintenance*, Tech. rep., Water Survey of Canada, Environment and Climate Change Canada, Ottawa, Ontario, Canada, originally

published 2002; Catalog No. En37-464/2016E-PDF (2016).
URL <https://publications.gc.ca/site/eng/9.898971/publication.html>

- [57] Government of Canada, Ice conditions warning, https://wateroffice.ec.gc.ca/ice_conditions_e.html, environment and Climate Change Canada, Water Survey of Canada. Accessed 2025-11-23 (2020).
- [58] B. Turcotte, B. Morse, A global river ice classification model, *Journal of Hydrology* 507 (2013) 134–148. doi:10.1016/j.jhydrol.2013.10.032.
- [59] S. Beltaos (Ed.), *River ice formation*, Committee on River Ice Processes and the Environment (CRIPE), Edmonton, AB, Canada, 2013.
- [60] World Meteorological Organization, *Manual on Stream Gauging*, Volume I: Fieldwork (2010).